The Astrophysical Journal Supplement Series, 139:439–465, 2002 April

THE STRUCTURE OF THE LOCAL INTERSTELLAR MEDIUM. I. HIGH-RESOLUTION OBSERVATIONS OF Fe II, Mg II, AND Ca II TOWARD STARS WITHIN 100 PARSECS

Seth Redfield
JILA, University of Colorado, Boulder, CO 80309; sredfiel@casa.colorado.edu

and

Jeffrey L. Linsky
JILA, University of Colorado and NIST, Boulder, CO 80309; jlinsky@jila.colorado.edu
Received 2001 September 20; accepted 2001 November 13

ABSTRACT

High-resolution absorption measurements ($\lambda/\Delta\lambda \gtrsim 100{,}000$) of the resonance lines of Fe II, Mg II, and Ca II are presented for all available observed targets within 100 pc. The Fe II and Mg II spectra were obtained with the Goddard High Resolution Spectrograph (GHRS) and the Space Telescope Imaging Spectrograph (STIS) instruments aboard the *Hubble Space Telescope* (*HST*). Of the 63 observations of targets within 100 pc, we present new measurements for 24 lines of sight. We also compiled all published absorption measurements based on Ca II spectra obtained by various ground-based instruments. For each observation we provide measurements of the central velocity, Doppler parameter, and column density for each absorption component. These three ions provide the best opportunity to measure the component velocity structure. Because these are the heaviest ions observed in absorption through the warm local interstellar medium (LISM), the narrow line widths minimize significant blending of components and allow for accurate measurements of the central velocity. We present a statistical analysis of the LISM absorption measurements, which provides an overview of some physical characteristics of warm clouds in the LISM, such as, temperature, turbulent velocity, ionization degree, and depletion. The complete collection and reduction of all LISM absorption measurements provides an important database for studying the structure of nearby warm clouds. Subsequent papers will present models for the morphology and physical properties of individual structures (clouds) in the LISM.

Subject headings: ISM: atoms — ISM: clouds — ISM: structure — stars: chromospheres — ultraviolet: ISM — ultraviolet: stars

On-line material: machine-readable tables

1. INTRODUCTION

The physical properties of the interstellar medium (ISM) are best measured by the analysis of absorption lines in the spectra of bright background sources. Because most resonance lines of prominent ions in the ISM fall in the UV, such measurements have to be made above the atmosphere. Advances in UV spectrograph technology have progressed to a point where high-quality spectra of ISM absorption can be obtained for many ions. Savage & Sembach (1996) provide a review of moderate- to high-resolution ISM observations obtained by the Goddard High Resolution Spectrograph (GHRS) on board the *Hubble Space Telescope* (*HST*). The targets used in their review range from 200 pc to 5 kpc and therefore show prominent absorption due to the large quantities of interstellar material along the distant sight lines. Discrete gas clouds are thought to be responsible for the absorption. Due to the large distance of the targets, many clouds are observed along the line of sight and are highly blended and often completely saturated, thereby providing little information about the physical properties of the individual clouds. However, short sight lines to nearby stars traverse few absorbing clouds and relatively small amounts of absorbing material, resulting in unsaturated absorption features often free of severe blends, and providing accurate measurements of the physical properties of the individual clouds in the local interstellar medium (LISM).

The morphology and physical properties of the LISM are being extensively studied but are still not fully understood. Cox & Reynolds (1987) and Frisch (1995) provide reviews of measurements and theoretical models of the LISM. Frisch (1995) includes detailed descriptions of UV observations of the LISM, including some of the very first high-resolution observations made with GHRS on board *HST*. Measurements made by earlier UV instruments typically did not have the spectral resolution to resolve individual velocity components. A survey of Mg II *h* and *k* lines, two of the most prominent ISM lines in the UV, was presented by Génova et al. (1990) using spectra obtained by the *International Ultraviolet Explorer* (*IUE*). Although the low spectral resolution prohibited the identification of multiple absorption components, analysis of these data did provide a general understanding of the distribution of nearby warm gas.

Although few ISM lines appear outside of the UV spectral range, those present in the optical waveband have been extensively studied. The two most prominent lines are the Ca II H and K and Na I D1 and D2 lines. Observations made of these lines have been very important in understanding the structure of the LISM. These observations are easily attainable from the ground and can utilize the latest instrumental technology. However, due to the complicated stellar emission in these lines, LISM absorption is difficult to detect in late-type stars. Therefore, a relatively modest number of early-type stars in solar neighborhood can be observed. These observational selection effects are discussed in § 3.

Surveys of ultrahigh-resolution ($\lambda/\Delta\lambda \gtrsim 10^6$) spectra of Ca II absorption lines include those of Vallerga et al. (1993) and Welty, Morton, & Hobbs (1996), and Welty, Hobbs, & Kulkarni (1994) and Welsh et al. (1994) provide a survey of Na I observations. The large number of sight lines observed in these surveys permit a statistical analysis of ISM characteristics. One result of this analysis was that Ca II and Na I absorption are probably sampling different parcels of gas. For example, almost all sight lines within 50 pc show Ca II LISM absorption, whereas very few of these same sight lines show Na I absorption. Presumably, Na I absorption is indicative of cold gas that exists beyond the Local Bubble (>50 pc), but Ca II samples warm gas that exists very nearby. Sfeir et al. (1999) use this assumption to map out the boundaries of the Local Bubble itself. Bertin et al. (1993) took a careful look at both Ca II and Na I, particularly toward nearby stars. Although eight of the 13 targets showed both Na I and Ca II absorption, these lines of sight contain the only detections of Na I absorption within 50 pc in all the Na I surveys. Accurate distance measurements of nearby stars, obtained by the *Hipparcos* satellite (Perryman et al. 1997) have been critical in providing the distance parameter in our investigation of the three-dimensional morphology of the LISM. Welsh, Crifo, & Lallement (1998) used the new *Hipparcos* distance measurements to refine their earlier analysis of the distribution of Na I gas in the ISM.

Physical properties of clouds in the LISM can be derived from a study of the entire set of observations along the many lines of sight that the high-resolution spectrographs on board *HST* have made during the last decade. Many authors have studied the kinematic structure of the LISM (Crutcher 1982; Lallement & Bertin 1992; Lallement et al. 1995). The simplest model for the structure of the complex of warm, partially ionized material in the LISM is that of individual clouds, which have unique values for their density, velocity, temperature, and abundances. Lallement & Bertin (1992) and Lallement et al. (1995) found a coherent velocity structure for the warm gas cloud that directly surrounds the solar system. They called this cloud the Local Interstellar Cloud (LIC). Since the LIC velocity vector agrees with the flow of material through the heliosphere and into the solar system as measured by Witte et al. (1993), the Sun must be located inside the LIC. The LIC velocity vector has also been successful in predicting central absorption velocities for many lines of sight through the LIC. Lallement & Bertin (1992) and Lallement et al. (1995) also found a coherent velocity structure for the Galactic (G) Cloud, located in the direction of the Galactic center. These kinematic models were based on only ~10 lines of sight. A three dimensional model of the LIC morphology was presented by Linsky et al. (2000) and Redfield & Linsky (2000) based on D I LISM absorption measurements along ~30 lines of sight. Redfield & Linsky 2001 then studied the small-scale structure of the LIC by analyzing the Mg II absorption toward 18 Hyades stars. The small angular distance between these stars permitted a comparative study of similar lines of sight and sampled LISM structure on scales $\lesssim$1.0 pc. Other physical properties of the LISM, such as depletions, temperature, turbulent velocity, and ionization structure have been analyzed for individual lines of sight but not yet for LISM clouds outside of the LIC. A collection of LISM measurements would allow for a large-scale analysis of the physical properties of the LISM. A high-resolution LISM absorption measurement survey, in the style of more distant ISM analyses in the UV (Savage & Sembach 1996) and in the optical (Vallerga et al. 1993; Welty et al. 1996), is the goal of this paper, and future papers. In this paper we present LISM measurements of Mg II, Fe II, and Ca II absorption for all available lines of sight toward stars located within 100 pc. We have chosen to analyze the heaviest ions first because they have the narrowest line widths, providing the most accurate measurements of the velocity structure along the lines of sight. These measurements will be useful in the analysis of the lighter ions that have broader line widths, which as a result, provide less information about the velocity structure of clouds along the line of sight. In § 2, we present new analyses of Mg II and Fe II spectra. We combine these measurements with all Mg II, Fe II, and Ca II LISM absorption line analyses from the literature. In § 3, we present the LISM absorption line measurements and investigate general characteristics of clouds in the warm LISM. In future papers we will describe the kinematics and morphology of several clouds in the LISM using the data presented in this paper.

2. OBSERVATIONS

We list in Table 1 all stars located within 100 pc which have high-resolution ($\lambda/\Delta\lambda \gtrsim 100{,}000$) spectra of the Mg II *h* and *k* lines (2803.5305 Å and 2796.5318 Å, respectively) and/or the Fe II lines (2600.1729 Å, 2586.6500 Å, 2382.7652 Å, 2374.4612 Å, 2344.2139 Å). For all 63 stars, the stellar spectral type, visible magnitude, stellar radial velocity, and Galactic coordinates are taken from the SIMBAD database unless otherwise noted. The *Hipparcos* distances (Perryman et al. 1997) are listed without errors. The errors in *Hipparcos* trigonometric parallax measurements for stars within 100 pc are small enough to have no influence on the interpretation of our results. In general, at 1 pc the 1 σ error in the distance is on the order of ~0.1 pc, at 30 pc the 1 σ error is ~1.0 pc, and at 100 pc the 1 σ error is ~5.0 pc. Also listed are the predicted absorption velocities for the LIC and G clouds computed using the vectors proposed by Lallement & Bertin (1992) and Lallement et al. (1995).

The Mg II and Fe II resonance lines lie in the ultraviolet and must therefore be observed above the atmosphere. The only space-based UV spectrographs, with resolution $\lesssim$3 km s^{-1} and with bandwidths that include these lines have been two instruments on board the *Hubble Space Telescope*: the Goddard High Resolution Spectrograph (GHRS) from 1990 April to 1997 February, and the Space Telescope Imaging Spectrograph (STIS) from 1997 February to the present. The GHRS instrument is described by Brandt et al. (1994) and Heap et al. (1995). Soderblom et al. (1994) describe improvements to the GHRS instrument for observations taken after the installation of the Corrective Optics Space Telescope Axial Replacement (COSTAR) in 1993 December. The STIS instrument is described by Kimble et al. (1998) and Woodgate et al. (1998). The broad spectral range of STIS available in its high-resolution modes is ideally suited for LISM absorption line studies. All high-resolution observations of nearby targets taken by the STIS instrument will likely contain important resonance lines that show ISM absorption by nearby gas.

Many *HST* observations of the stars listed in Table 1 were taken for the express purpose of studying the structure of the LISM along these sight lines. However, more than a

TABLE 1

PARAMETERS FOR STARS WITHIN 100 pc WITH Mg II OR Fe II HIGH-RESOLUTION SPECTRA

HD Number	Other Name	Spectral Type	m_V	v_R (km s^{-1})	l (deg)	b (deg)	Distance[a] (pc)	v_{LIC}[b] (km s^{-1})	v_G[c] (km s^{-1})
128620	α Cen A	G2 V	−0.0	−24.6	315.7	−0.7	1.3	−15.6	−18.0
128621	α Cen B	K1 V	1.3	−20.7	315.7	−0.7	1.3	−15.6	−18.0
48915	α CMa	A1 V	−1.5	−7.6	227.2	−8.9	2.6	19.5	21.6
22049	ϵ Eri	K2 V	3.7	15.5	195.8	−48.1	3.2	21.6	25.7
201091	61 Cyg A	K5 V	5.2	−64.3	82.3	−5.8	3.5	−5.1	−4.7
61421	α CMi	F5 V	0.3	−3.2	213.7	13.0	3.5	19.7	21.1
26965	40 Eri A	K1 V	4.4	−42.2	200.8	−38.1	5.0	23.2	27.2
165341	70 Oph	K0 V	4.0	−6.9[d]	29.9	11.4	5.1	−23.5	−26.4
187642	α Aql	A7 V	0.8	−26.1	47.7	−8.9	5.1	−17.1	−18.2
155886	36 Oph A	K0 V	5.3	−0.6	358.3	6.9	5.5	−25.2	−28.4
131156A...	ξ Boo A	G8 V	4.7	3.0	23.1	61.4	6.7	−17.7	−21.5
216956	α PsA	A3 V	1.2	6.5	20.5	−64.9	7.7	−3.6	−1.9
172167	α Lyr	A0 V	0.0	−13.9	67.5	19.2	7.8	−13.5	−15.2
39587	χ^1 Ori	G0 V	4.4	−13.5	188.5	−2.7	8.7	24.9	27.9
20630	κ^1 Cet	G5 V	4.8	19.9	178.2	−43.1	9.2	22.8	27.0
197481	AU Mic	M0	8.6	1.2	12.7	−36.8	9.9	−15.3	−15.7
62509	β Gem	K0 III	1.2	3.3	192.2	23.4	10.3	19.6	21.0
102647	β Leo	A3 V	2.1	−0.2	250.6	70.8	11.1	−3.4	−6.1
124897	α Boo	K1.5 III	−0.0	−5.2	15.1	69.1	11.3	−15.5	−19.3
33262	ζ Dor	F7 V	4.7	−2.0	266.0	−36.7	11.7	7.8	9.4
34029	α Aur	G5 III	0.1	30.2	162.6	4.6	12.9	22.0	24.6
36705	AB Dor	K1 III	6.9	33[e]	275.3	−33.1	14.9	4.3	5.3
128167	σ Boo	F2 V	4.5	0.2	45.6	67.2	15.5	−14.1	−17.5
432.....	β Cas	F2 IV	2.3	11.3	117.5	−3.3	16.7	9.4	11.3
23754	τ^6 Eri	F4 V	4.2	6.5	217.4	−50.3	17.9	19.0	22.7
39060	β Pic	A5 V	3.9	20	258.4	−30.6	19.3	10.1	11.8
11443	α Tri	F6 IV	3.4	−12.6	138.6	−31.4	19.7	18.0	21.7
29139	α Tau	K5 III	0.9	54.3	181.0	−20.3	20.0	25.5	29.4
108903	γ Cru A	M3.5 III	1.6	21.4	300.2	5.7	27.0	−10.7	−12.9
22468	V711 Tau	G9 V	5.9	−23	184.9	−41.6	29.0	23.3	27.4
4128	β Cet	K0 III	2.0	13.0	111.3	−80.7	29.4	8.2	11.4
8538	δ Cas	A5 IV	2.7	6.7	127.2	−2.4	30.5	13.0	15.3
120315	η UMa	B3 V	1.9	−10.9	100.7	65.3	30.9	−5.8	−8.1
209952	α Gru	B7 IV	1.7	11.8	350.0	−52.5	31.1	−8.7	−8.1
155555	V824 Ara	K1 V	6.8	2.3	324.9	−16.3	31.4	−15.8	−17.5
	HZ 43	Daw	12.7	62.0[f]	54.1	84.2	32.0	−8.9	−12.0
82210	DK UMa	G4 IV	4.6	−27.2	142.6	38.9	32.4	9.4	9.5
80007	β Car	A2 IV	1.7	−5	286.0	−14.4	34.1	−2.3	−2.8
62044	σ Gem	K1 III	4.3	45.8	191.2	23.3	37.5	19.7	21.0
215789	ϵ Gru	A3 V	3.5	0	338.3	−56.5	39.7	−6.0	−5.1
27808	SAO 76593	F8 V	7.1	38.9	174.8	−19.1	40.9	25.2	29.0
28568	SAO 93981	F5 V	6.5	40.9	180.5	−21.4	41.2	25.5	29.3
26345	SAO 93801	F6 V	6.6	37.1	175.2	−23.6	43.1	25.1	29.0
28736	SAO 111879	F5 V	6.4	39.8	190.2	−27.6	43.2	25.2	29.1
31845	101 Tau	F5 V	6.8	42.5	185.1	−16.0	43.3	25.7	29.3
29225	SAO 94033	F5 V	6.6	33.7	181.6	−20.5	43.5	25.6	29.4
28608	SAO 93982	F5	7.0	41.4	185.1	−24.7	43.6	25.4	29.3
29419	SAO 76683	F5	7.5	39.9	176.0	−15.6	44.2	25.3	29.0
164058	γ Dra	K5 III	2.2	−27.6	79.1	29.2	45.2	−9.8	−11.4
28205	V993 Tau	F8 V	7.4	39.3	180.4	−22.4	45.8	25.4	29.3
28406	SAO 93963	F6 V	6.9	38.6	178.8	−20.6	46.3	25.4	29.3
28033	SAO 76609	F8 V	7.4	38.8	175.4	−18.9	46.4	25.3	29.1
28237	SAO 93945	F8	7.5	40.2	183.7	−24.7	47.2	25.4	29.3
26784	SAO 93831	F8 V	7.1	38.5	182.4	−27.9	47.4	25.1	29.1
21847	SAO 56530	F8	7.3	...	156.2	−16.6	48.9	22.6	26.2
28483	SAO 93973	F6 V	7.1	38.0	177.3	−19.2	50.2	25.4	29.2
27561	SAO 93885	F5 V	6.6	39.2	180.4	−24.3	51.4	25.3	29.3
30738	SAO 94162	F8	7.3	42.7	183.5	−17.6	51.8	25.7	29.4
220657	υ Peg	F8 IV	4.4	−11.1	98.6	−35.4	53.1	5.1	7.6
27848	SAO 93913	F6 V	7.0	40.1	178.6	−22.0	53.4	25.4	29.3
203387	ι Cap	G8 III	4.3	11.5	33.6	−40.8	66.1	−11.8	−11.5
	G191-B2B	Daw	11.6	5[g]	156.0	7.1	68.8	20.3	22.7
111812	31 Com	G0 III	4.9	−1.4	115.0	89.6	94.2	−7.2	−10.2

[a] *Hipparcos* distances (Perryman et al. 1997).
[b] Predicted projected LIC velocity from Lallement & Bertin 1992.
[c] Predicted projected G velocity from Lallement & Bertin 1992.
[d] Duflot, Figon, & Meyssonnier 1995.
[e] Brandt et al. 2001.
[f] Vennes & Thorstensen 1994.
[g] Reid & Wegner 1988.

third of the observations along lines of sight listed in Table 1 were taken for other purposes. We list in Table 2 the *HST* observations of those stars with LISM absorption that have not been published. All of these data were taken from the *HST* Data Archive and are publicly available. The data reduction procedure for the observations listed in Table 2 is described in § 2.1, and the spectral analysis is discussed in § 2.2.

2.1. *Data Reduction*

We reduced the GHRS data acquired from the *HST* Data Archive with the CALHRS software package using the Image Reduction and Analysis Facility (IRAF) and the Space Telescope Science Data Analysis System (STSDAS). The most recent reference files were used in the reduction. In many cases, the current reference files produced an

TABLE 2
HST Observational Parameters

HD Number	Other Name	Instrument	Grating	Spectral Range (Å)	Resolution ($\lambda/\Delta\lambda$)	Exposure Time (s)	PI Name	Program ID	Date
128621	α Cen B	GHRS	ECH-B	2594–2606	100000	979.2	LINSKY	3943	1993 Apr 29
22049	ϵ Eri	STIS	E230H	2574–2846	113000	180.0	JORDAN	7479	2000 Mar 17
165341	70 Oph	STIS	E230H	2524–2796	114000	1000.0	AYRES	8280	2000 Aug 23
		STIS	E230H	2724–2995	114000	378.0	AYRES	8280	2000 Aug 23
131156A...	ξ Boo A	GHRS	ECH-B	2792–2807	100000	108.8	JORDAN	6076	1996 Aug 18
		GHRS	ECH-B	2792–2807	100000	108.8	JORDAN	6076	1996 Aug 20
		GHRS	ECH-B	2792–2807	100000	217.6	JORDAN	6076	1996 Aug 22
39587	χ^1 Ori	STIS	E230H	2524–2796	114000	1000.0	AYRES	8280	2000 Oct 3
		STIS	E230H	2724–2995	114000	480.0	AYRES	8280	2000 Oct 3
20630	κ^1 Cet	STIS	E230H	2524–2796	114000	1000.0	AYRES	8280	2000 Sep 19
		STIS	E230H	2724–2995	114000	378.0	AYRES	8280	2000 Sep 19
197481	Au Mic	GHRS	ECH-B	2792–2807	100000	979.2	LINSKY	4234	1992 Sep 10
62509	β Gem	STIS	E230H	2224–2496	114000	2304.0	JORDAN	8294	2000 Apr 10
102647	β Leo	GHRS	ECH-B	2340–2352	100000	403.2	FERLET	2537	1992 Jan 23
		GHRS	ECH-B	2590–2603	100000	633.6	FERLET	2537	1992 Jan 23
124897	α Boo	STIS	E230H	2574–2846	114000	1340.0	AYRES	7733	1998 Aug 24
33262	ζ Dor	STIS	E230H	2524–2796	114000	800.0	AYRES	8280	1999 May 1
		STIS	E230H	2724–2995	114000	255.0	AYRES	8280	1999 May 1
128167	σ Boo	STIS	E230H	2374–2646	114000	1200.0	HEAP	7433	1999 Apr 28
		STIS	E230H	2624–2895	114000	1079.0	HEAP	7433	1999 Apr 28
		STIS	E230H	2974–3145	114000	1440.0	HEAP	7433	1999 Apr 28
23754	τ^6 Eri	STIS	E230H	2374–2646	114000	1200.0	HEAP	7433	1998 Dec 27
		STIS	E230H	2624–2895	114000	1062.0	HEAP	7433	1998 Dec 27
		STIS	E230H	2874–3145	114000	1440.0	HEAP	7433	1998 Dec 27
39060	β Pic	STIS	E230H	2124–2396	114000	288.0	LAGRANGE	7512	1997 Dec 6
		STIS	E230H	2374–2646	114000	360.0	LAGRANGE	7512	1997 Dec 6
		STIS	E230H	2624–2895	114000	360.0	LAGRANGE	7512	1997 Dec 6
		STIS	E230H	2124–2396	114000	288.0	LAGRANGE	7512	1997 Dec 19
		STIS	E230H	2374–2646	114000	360.0	LAGRANGE	7512	1997 Dec 19
		STIS	E230H	2624–2895	114000	360.0	LAGRANGE	7512	1997 Dec 19
29139	α Tau	GHRS	ECH-B	2791–2806	100000	870.4	CARPENTER	5358	1994 Apr 8
		GHRS	ECH-B	2791–2807	100000	761.6	CARPENTER	6722	1996 Oct 15
22468	HR1099	GHRS	ECH-B	2594–2606	100000	979.2	LINSKY	4874	1993 Sep 19
120315	Alcaid	GHRS	ECH-B	2591–2604	100000	217.6	FRISCH	6886	1997 Jan 26
		GHRS	ECH-B	2790–2805	100000	108.8	FRISCH	6886	1997 Jan 26
209952	α Gru	GHRS	ECH-B	2365–2377	100000	217.6	SMITH	3941	1993 Jul 24
		GHRS	ECH-B	2590–2603	100000	217.6	SMITH	3941	1993 Jul 24
		GHRS	ECH-B	2791–2806	100000	108.8	SMITH	3941	1993 Jul 24
	HZ 43	GHRS	ECH-B	2376–2387	100000	2176.0	LANDSMAN	5884	1995 Jul 30
		GHRS	ECH-B	2792–2807	100000	2176.0	LANDSMAN	5884	1995 Jul 30
82210	DK UMa	STIS	E230H	2524–2796	114000	1500.0	AYRES	8280	2000 Feb 24
		STIS	E230H	2724–2995	114000	515.0	AYRES	8280	2000 Feb 24
80007	β Car	GHRS	ECH-B	2339–2352	100000	230.4	FERLET	2537	1993 Feb 9
		GHRS	ECH-B	2590–2603	100000	403.2	FERLET	2537	1993 Feb 9
		GHRS	ECH-B	2847–2861	100000	1555.2	FERLET	2537	1993 Feb 9
164058	γ Dra	GHRS	ECH-B	2793–2808	100000	108.8	CARPENTER	1362	1991 Apr 18
		GHRS	ECH-B	2791–2806	100000	217.6	BROWN	6068	1995 Jul 19
220657	υ Peg	STIS	E230H	2524–2796	114000	1460.0	AYRES	8280	2000 Jul 11
		STIS	E230H	2724–2995	114000	499.0	AYRES	8280	2000 Jul 11
203387	ι Cap	STIS	E230H	2524–2796	114000	1200.0	AYRES	8280	2000 Apr 15
		STIS	E230H	2724–2995	114000	480.0	AYRES	8280	2000 Apr 15

improvement in data quality, compared to data reduced with reference files contemporaneous with the observations. Many of the echelle observations were obtained in the FP-SPLIT mode to reduce fixed-pattern noise. The individual readouts of the FP-SPLIT spectra were combined using a cross-correlation procedure called HRS_MERGE (Robinson et al. 1992). The reduction included assignment of wavelengths using calibration spectra obtained during the course of the observations. The calibration spectra include either a WAVECAL, a direct Pt-Ne lamp spectrum from which a dispersion relation can be obtained, or a SPYBAL (Spectrum Y-Balance), from which only a zero-point offset can be obtained. Any significant errors involved in the wavelength calibration are included in our central velocity determinations discussed in § 3.1.

We reduced the STIS data acquired from the *HST* Data Archive using the STIS team's CALSTIS software package written in IDL (Lindler 1999). The reduction included assignment of wavelengths using calibration spectra obtained during the course of the observations. The ECHELLE_SCAT routine in the CALSTIS software package was used to remove scattered light. However, the scattered light contribution is negligible in this spectral range and does not influence the uncertainties in our spectral analysis.

2.2. *Spectral Analysis*

Figure 1 shows the Mg II and Fe II lines observed for the 22 lines of sight listed in Table 2 that have not yet been published. All spectra are shown with a heliocentric velocity scale, together with the best fits to the absorption by each interstellar component (*dashed lines*), and the total interstellar absorption convolved with the instrumental profile (*thick solid lines*).

When interstellar absorption is measured against a stellar emission line, the placement of the "continuum" flux against which one measures the interstellar absorption features requires an estimate of the emission line flux at the absorption line wavelength. Because the wavelength of the absorption is different for each line of sight, the placement of the unobserved stellar flux for some cases can be difficult and be the dominant source of error. In most cases, the continuum can be determined in a straightforward manner by fitting a polynomial to spectral regions just blueward and redward of the interstellar absorption. Another technique for estimating the unobserved stellar flux involves flipping the emission line about the stellar rest frame. If the interstellar absorption is far from line center, this technique can be very useful in estimating the stellar flux. When the placement of the unobserved stellar flux is particularly complicated, we use multiple continua and incorporate the various results into our error estimates. Our estimated stellar emission is shown by the thin solid lines in Figure 1.

Once the stellar emission line profiles have been estimated, we fit the interstellar absorption using standard techniques (Linsky & Wood 1996; Piskunov et al. 1997; Dring et al. 1997). We start with only one absorption component in the fit and increase the number of components as the data warrant, and the quality of the fit improves. While, additional weak absorption components could be present, they do not appear in the data much above the level of noise and thereby do not significantly influence the χ^2 metric. Therefore, we fit the spectra with the lowest number of absorption components that allow for an acceptable fit. The rest wavelengths and oscillator strengths of the lines used in our fits are taken from Morton (1991), and we use Voigt functions to represent the opacity profiles of the fitted interstellar absorption. The dashed lines in Figure 1 are the absorption line fits before convolution with the instrumental line spread function. The thick solid lines indicate the absorption features with the instrumental broadening applied. The instrumental line spread functions assumed in our fits for GHRS spectra are taken from Gilliland (1994) and for STIS spectra from Sahu et al. (1999).

We fit all lines of each ion simultaneously in order to glean all available absorption information from the data. The difference in oscillator strengths between the various lines can be very useful in constraining the interstellar parameters, the stellar continuum level, and the number of absorption components. For example, the Mg II k line for υ Peg (Fig. 1*g*) is very saturated, making it difficult to determine unique values for the interstellar column density and Doppler parameter. However, the less opaque Mg II h, and especially the less opaque Fe II lines show weaker, unsaturated interstellar absorption lines. Simultaneously fitting all lines allows us to determine the interstellar absorption parameters more accurately than by fitting only one of the lines. We fit each line separately as well, to see how much the parameters change, allowing us to estimate the systematic errors involved in our fits and to determine the uncertainties in the various fit parameters more accurately. In most cases, the systematic errors, such as the stellar emission line continuum placement, dominates the statistical errors. Therefore, our 1 σ error bars include both statistical and systematic errors.

Tables 3 and 4 list the interstellar absorption parameters and 1 σ errors for all targets in Table 1 that show interstellar absorption. This includes our fits to the 22 lines of sight shown in Figure 1. Table 3 lists all LISM measurements of Mg II h and k lines and Table 4 lists all LISM measurements of Fe II lines.

LISM absorption is not visible toward some nearby stars because of particular stellar properties. The nearby A-star, β Pic, has a prominent circumstellar disk and has been frequently observed to investigate possible proto–planetary formation for comparison with the formation of our own Solar System (Artymowicz 1997; Vidal-Madjar, Lecavelier des Etangs, & Ferlet 1998). The circumstellar material around β Pic is a major absorber along that line of sight. Although Mg II spectra exist, the LISM absorption line is so broad that it merges with the very broad circumstellar material absorption and is indistinguishable from it (Vidal-Madjar et al. 1994). We therefore include no entry for β Pic in Table 3. However, the Fe II LISM absorption lines are narrow enough to be distinguished from the circumstellar material absorption. This was first noted by Lallement et al. (1995), who fitted the blue side of the LISM absorption. The results of this analysis are given in Table 4. New STIS observations confirm that this is a stable absorption feature, supporting the claim that it is LISM absorption and not variable circumstellar absorption. The STIS data also provide additional Fe II lines for analysis, and we have included them here. The results are listed in Table 4.

Prominent stellar winds can also be responsible for erasing the spectral signature of LISM absorption. The K giant α Tau and the M giant γ Cru A both have prominent P Cygni stellar wind profiles in their Mg II lines. Only Mg II

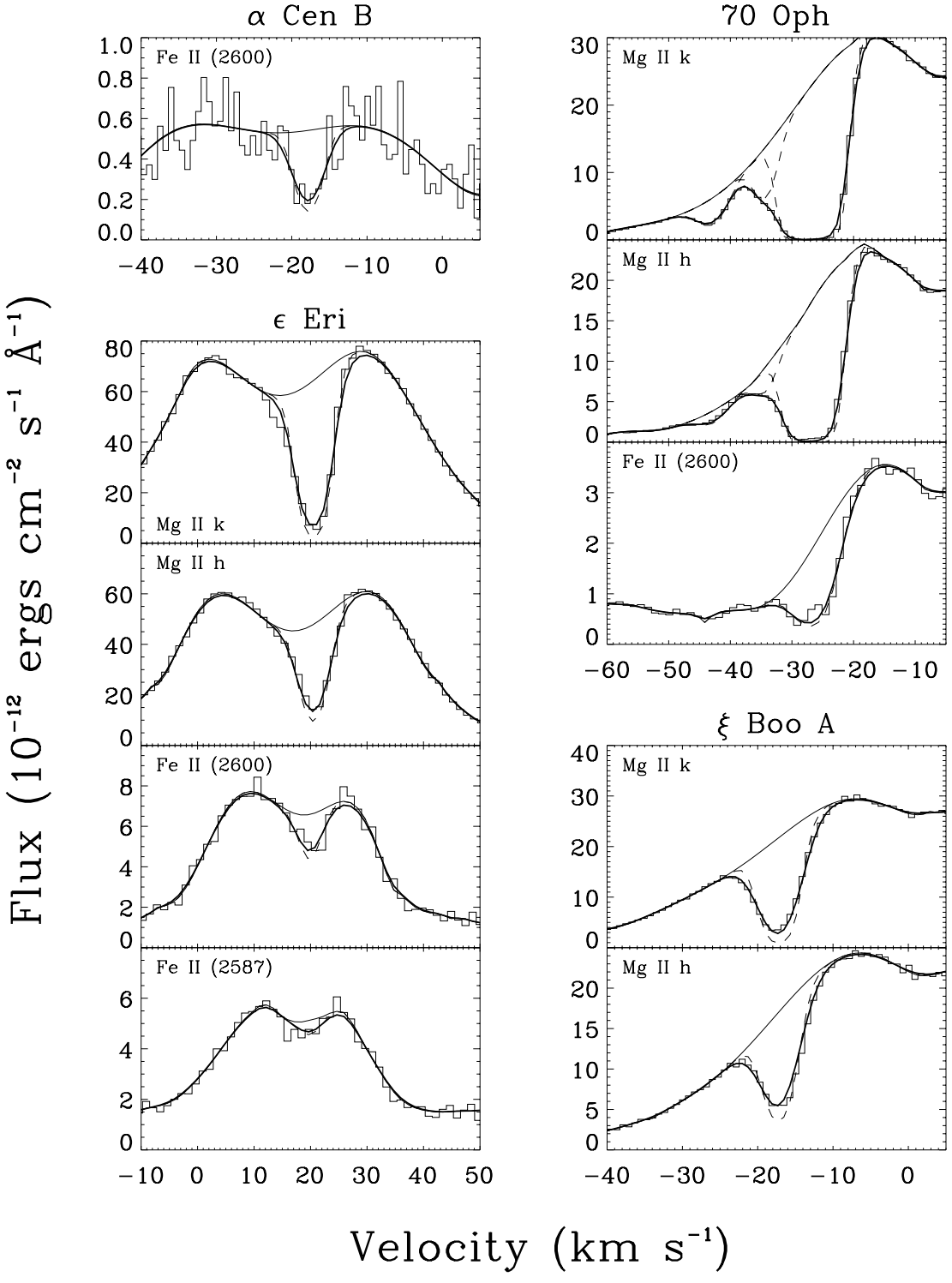

FIG. 1.—Our best fits to the Mg II and Fe II lines for 22 lines of sight listed in Table 2. The name of the target star is given above each group of plots, and the resonance line is identified within each individual plot. The data are shown in histogram form. The thin solid lines are our estimates for the missing stellar flux across the absorption lines. The dashed lines are the best-fit individual absorption lines before convolution with the instrumental profile. The thick solid line represents the combined absorption fit after convolution with the instrumental profile. The spectra are plotted vs. heliocentric velocity. The parameters for these fits are given in Table 3 for Mg II and in Table 4 for Fe II.

spectra are available for α Tau (Robinson, Carpenter, & Brown 1998). These authors note that although the broad P Cygni profile prevents detection of LISM absorption at velocities predicted for the LIC and G clouds, there is an absorption feature detected at very high velocities, before the wind absorption completely saturates. Based on the 2 year stability of this absorption feature and the fact that its wavelength corresponds to the high radial velocity of the star, Robinson et al. (1998) proposed that it is caused by a collection of material where the stellar wind interacts with the ISM. This phenomenon has been observed in the Lyα line of hydrogen for the heliosphere and for astrospheres

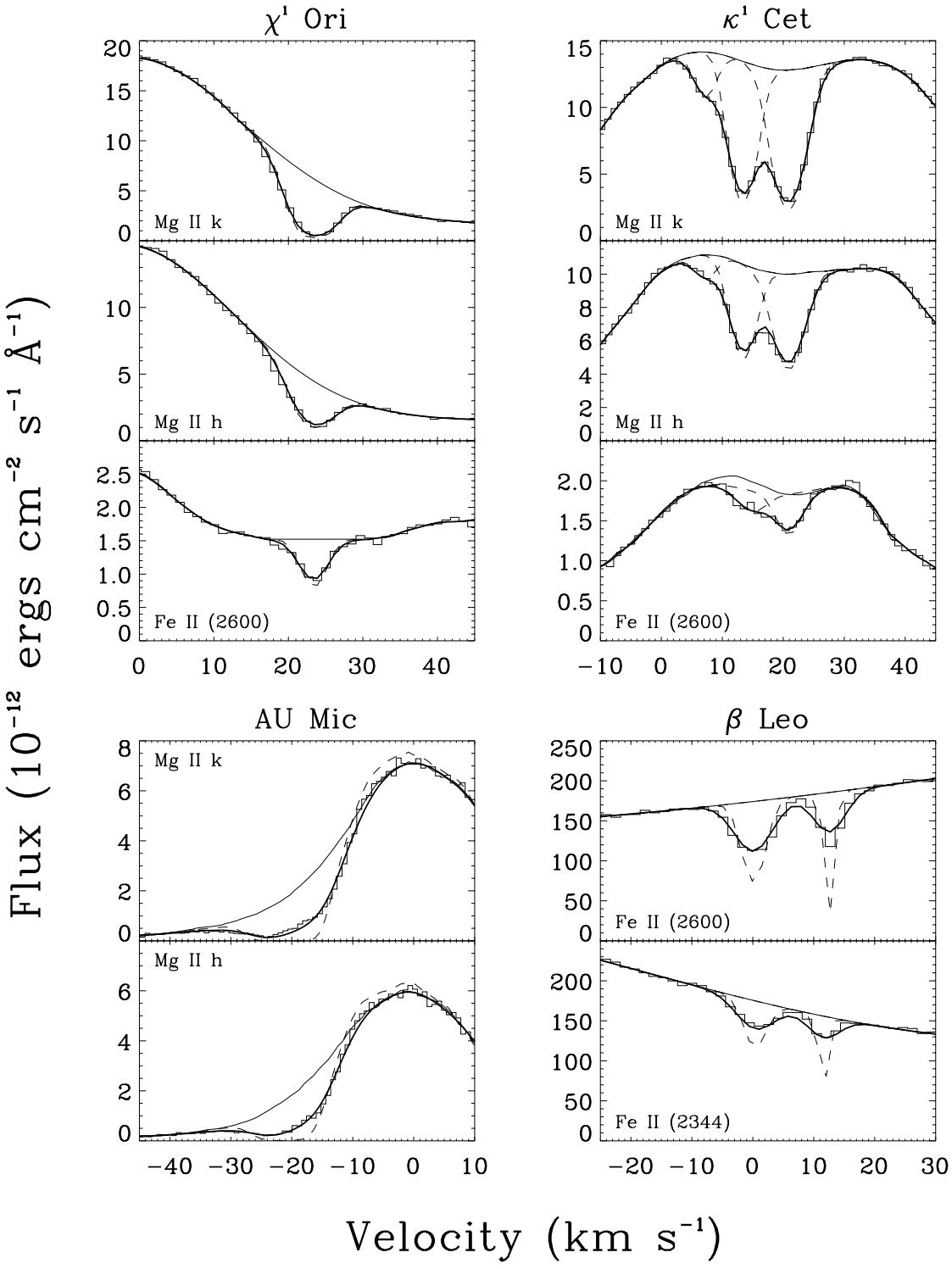

FIG. 1.—*Continued*

around other stars (Linsky & Wood 1996; Wood, Müller, & Zank 2000). We have included an absorption line analysis for α Tau in Table 3 for completeness. Although the Doppler parameter and Mg II column density are not atypical for LISM absorption (see §§ 3.2 and 3.3), the high central velocity of the absorption feature and its correspondence with the radial velocity of the star make it unlikely that the source of the absorption is located in the LISM (see § 3.1). Both Fe II and Mg II spectra for γ Cru A have broad P Cygni profiles that do not permit any LISM absorption detection (Robinson & Carpenter 1995; Carpenter, Robinson, & Judge 1995). As a result, no entries for γ Cru A are included in Tables 3 and 4.

When a line is highly saturated, very little information about the absorbing material can be deduced. The K giant γ Dra has a prominent stellar wind, and the Mg II spectra exhibits a broad P Cyngi profile, as discussed above. However, LISM absorption is very clearly separated from the

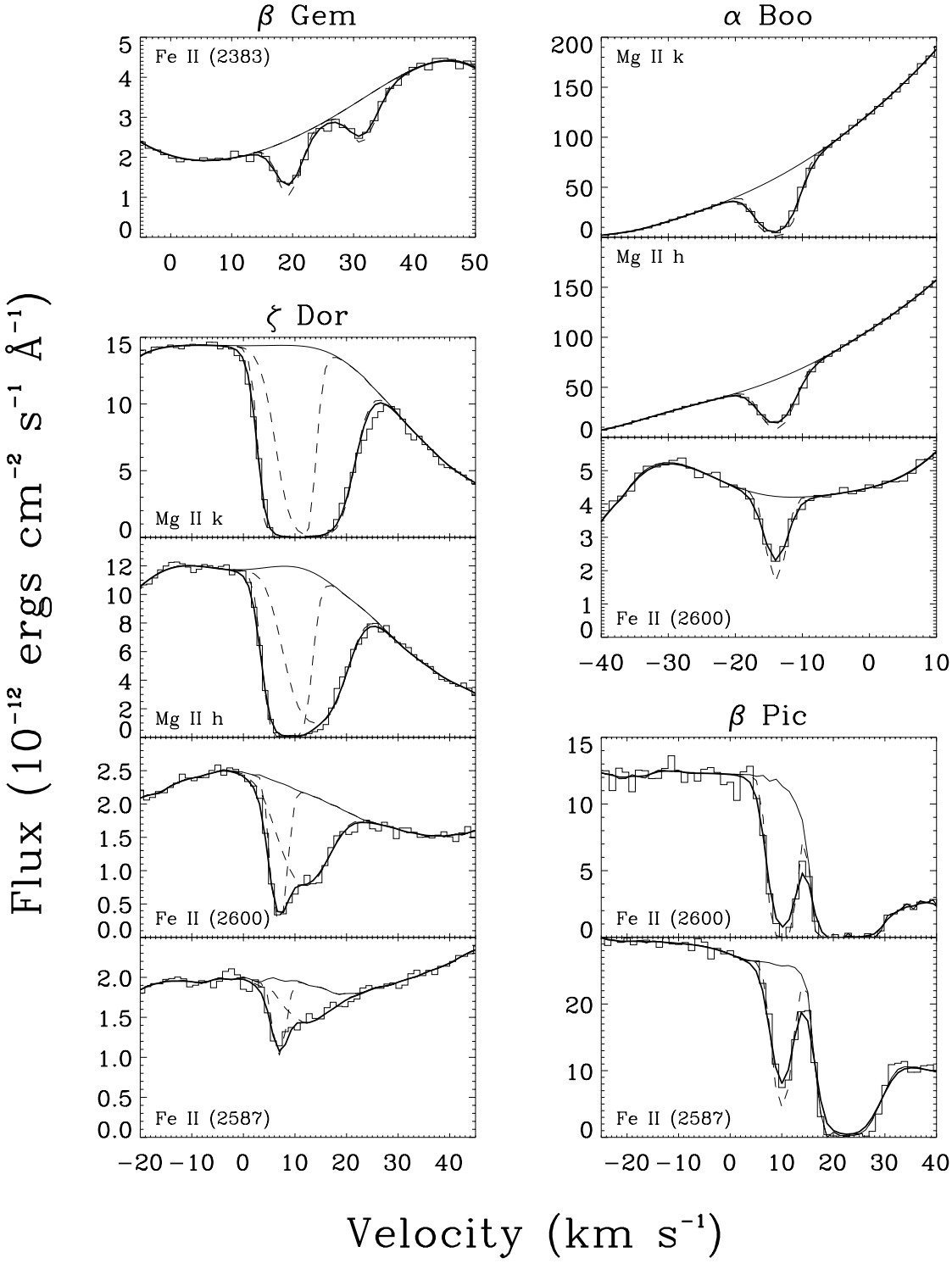

FIG. 1.—*Continued*

wind profile (Robinson & Carpenter 1995). The difficulty is that both Mg II lines are completely saturated, and no observations of the less opaque lines of Fe II are available to disentangle the velocity structure of the LISM absorption. Only the range of LISM absorption velocities and a lower limit to the total Mg II column density is provided in Table 3. This is an excellent demonstration that the Fe II lines, with their lower opacity and narrower line widths, can be vitally important in the analysis of LISM absorption.

The RS CVn binary HR 1099 (V711 Tau) shows clear Mg II LISM absorption analyzed by Piskunov et al. (1997) and listed in Table 3. The low signal-to-noise (S/N $\sim$ 5) Fe II spectra does not show any obvious LISM absorption but can provide the upper limit to the total Fe II column density listed in Table 4.

For each absorption component there are three fit parameters: the central velocity (v [km s^{-1}]), the Doppler width (b [km s^{-1}]), and the column density (log $N_{\rm ion}$ [log (cm^{-2})]).

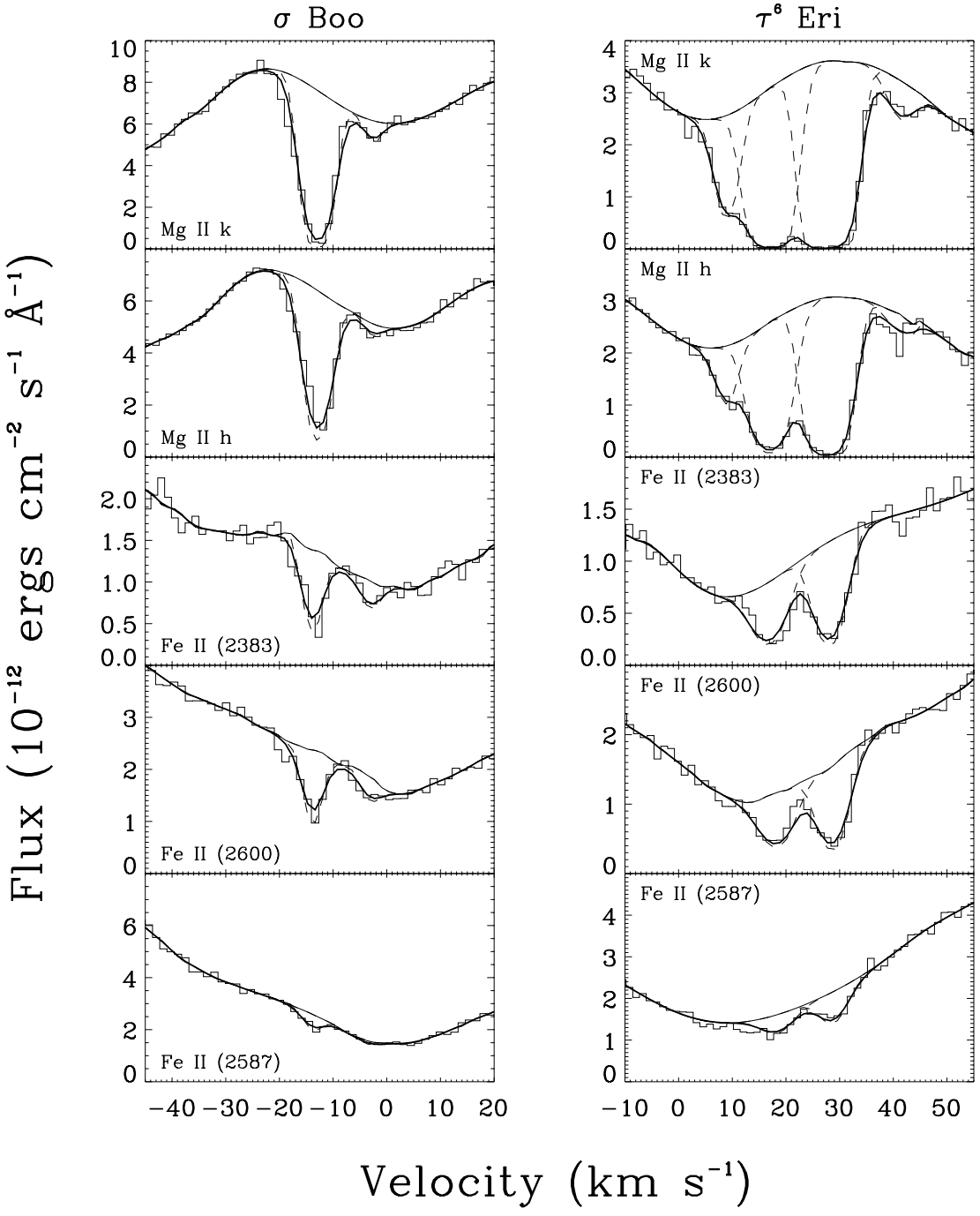

FIG. 1.—*Continued*

The central velocity corresponds to the mean projected velocity of the absorbing material along the line of sight to the star. If we assume as a first approximation that the warm partially ionized material in the solar neighborhood exists in small, homogeneous cloudlets each moving with a single bulk velocity, then each absorption component will correspond to a single cloudlet, and its velocity is the projection of its three-dimensional velocity vector. The Doppler parameter is related to the temperature (T [K]) and nonthermal velocity (ξ [km s^{-1}]) of the interstellar material by the following equation:

$$b^2 = \frac{2kT}{m} + \xi^2 = 0.016629\frac{T}{A} + \xi^2 \,, \qquad (1)$$

where k is Boltzmann's constant, m is the mass of the ion observed, and A is the atomic weight of the element in atomic mass units ($A_{\rm Mg} = 24.305$, $A_{\rm Ca} = 40.078$, $A_{\rm Fe} = 55.847$). Because of the large atomic weight of Mg, Ca, and Fe, their Doppler parameters are more sensitive to

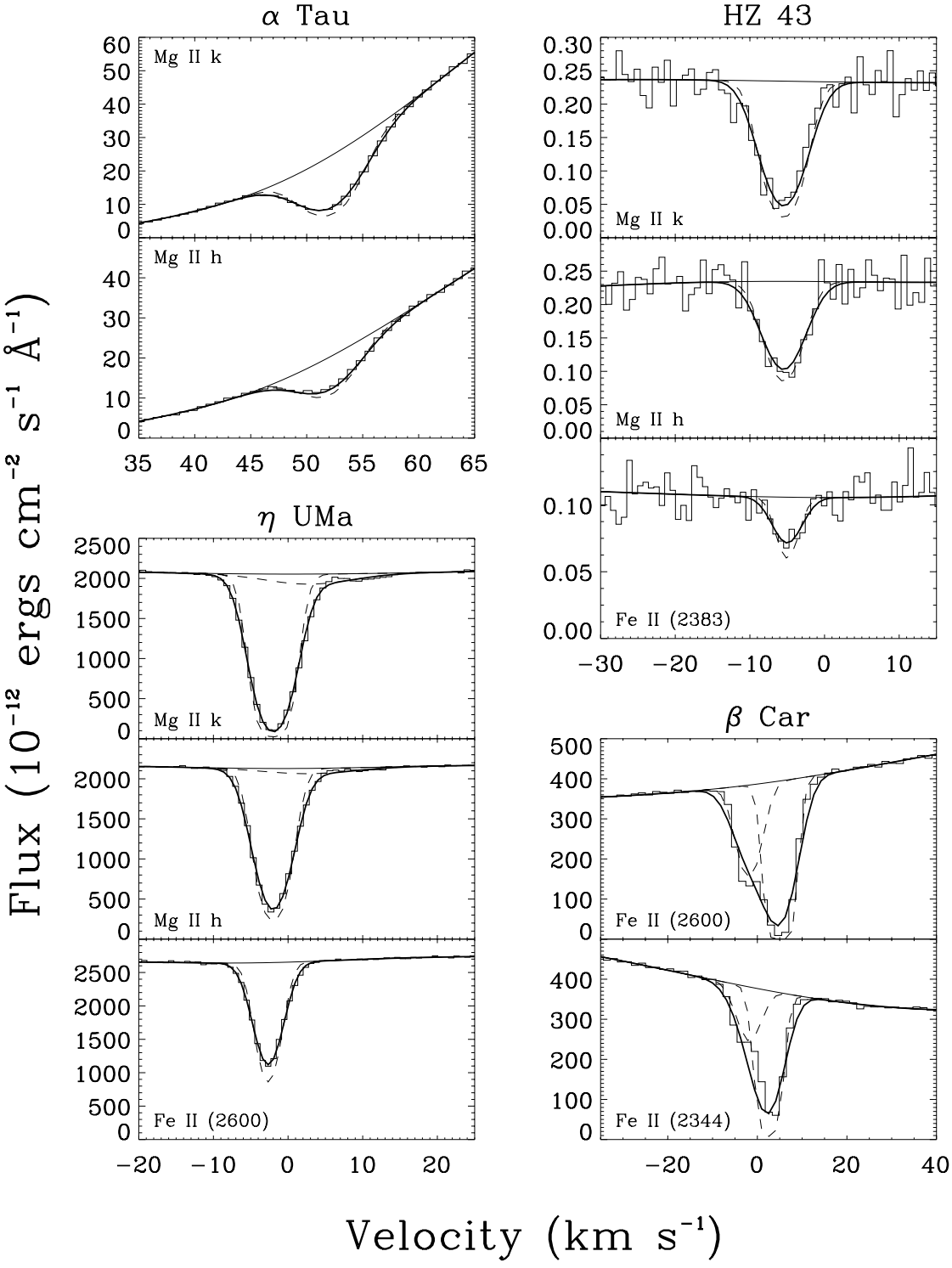

FIG. 1.—*Continued*

changes in turbulent velocity than temperature. The column density is a measure of the amount of material along the line of sight to the star. If we assume homogeneous cloudlets with constant density, the column density will be directly proportional to the cloud thickness. The compilation of all measurements for stars within 100 pc provides an important database for the analysis of the structure of the LISM. The velocity structure is discussed in § 3.1, the Doppler parameter structure is discussed in § 3.2, and the column density structure is discussed in § 3.3.

3. DISCUSSION

The following discussion will primarily be a statistical analysis of the LISM absorption fit parameters discussed above. In future papers we will present more detailed analy-

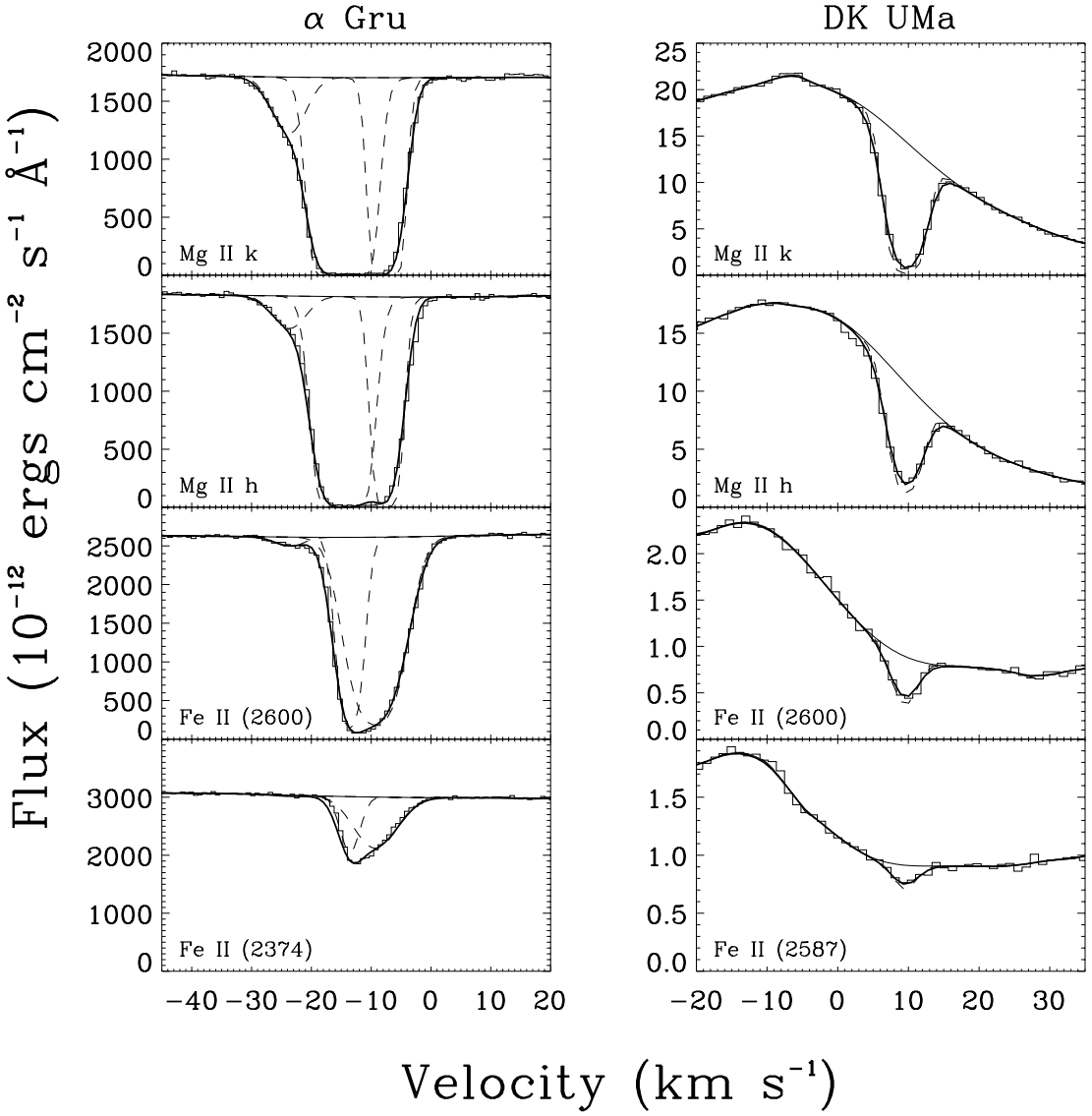

FIG. 1.—*Continued*

ses of the database, including the morphology, kinematics, and physical properties of identifiable structures (i.e., clouds) in the LISM.

Resonance lines at optical wavelengths also provide valuable information regarding the warm LISM gas. A large collection of observations exist for the strongest lines in the optical: Ca II H and K (3969.5901 Å and 3934.7750 Å, respectively) and Na I D1 and D2 (5897.5581 Å and 5891.5833 Å, respectively). However, the Na I absorption traces cold gas, predominantly outside the Local Bubble (Sfeir et al. 1999; Welty et al. 1996; Welsh et al. 1994). Ca II absorption, however, does trace the nearby warm gas along with Mg II and Fe II. Since the atomic weight of Ca is intermediate between Mg and Fe, it is appropriate to include Ca II observations in our analysis of the heavy ions. The stellar parameters of all stars within 100 pc that have high-resolution ($\lambda/\Delta\lambda \gtrsim 100{,}000$) spectra of the Ca II lines are listed in Table 5, following the format of Table 1. The interstellar absorption fit parameters for all 53 stars listed in Table 5 are provided in Table 6, following the format of Tables 3 and 4. All interstellar fit parameters for Ca II targets were taken from the literature. The location of all stars listed in Tables 1 and 5 are shown in Galactic coordinates in Figure 2. All *HST* targets with spectra of Mg II and Fe II are indicated by circles. Those stars with spectra analyzed in this paper are shown in Figure 1 by filled circles, while those lines of sight previously analyzed and published are indicated by open circles. All Ca II targets listed in Table 5 are indicated by the symbol "×." Although spatial coverage overall is fairly good, there are areas of the sky that are undersampled, while others are densely sampled. For example, the Hyades sample (Redfield & Linsky 2001) includes observations of 18 members of the Hyades star cluster, all $\lesssim 10°$ apart, located at $l \sim 180°$. However, there are very few UV observations toward the Galactic center, centered at $l \sim 300°$ and $b \sim 30°$. This is also the direction of the G Cloud, the nearest LISM cloud beyond the LIC. Although observations of Ca II absorption can provide velocity information, UV observations are necessary to measure other important physical properties of the gas such as, temperature, turbulent velocity, and degree of ionization. Note that there are only seven targets with both Mg II/Fe II and Ca II observations: α Cen A, α Aql, α PsA, δ Cas, η UMa, α Gru, and ϵ Gru. In the following sections we look at the statistical

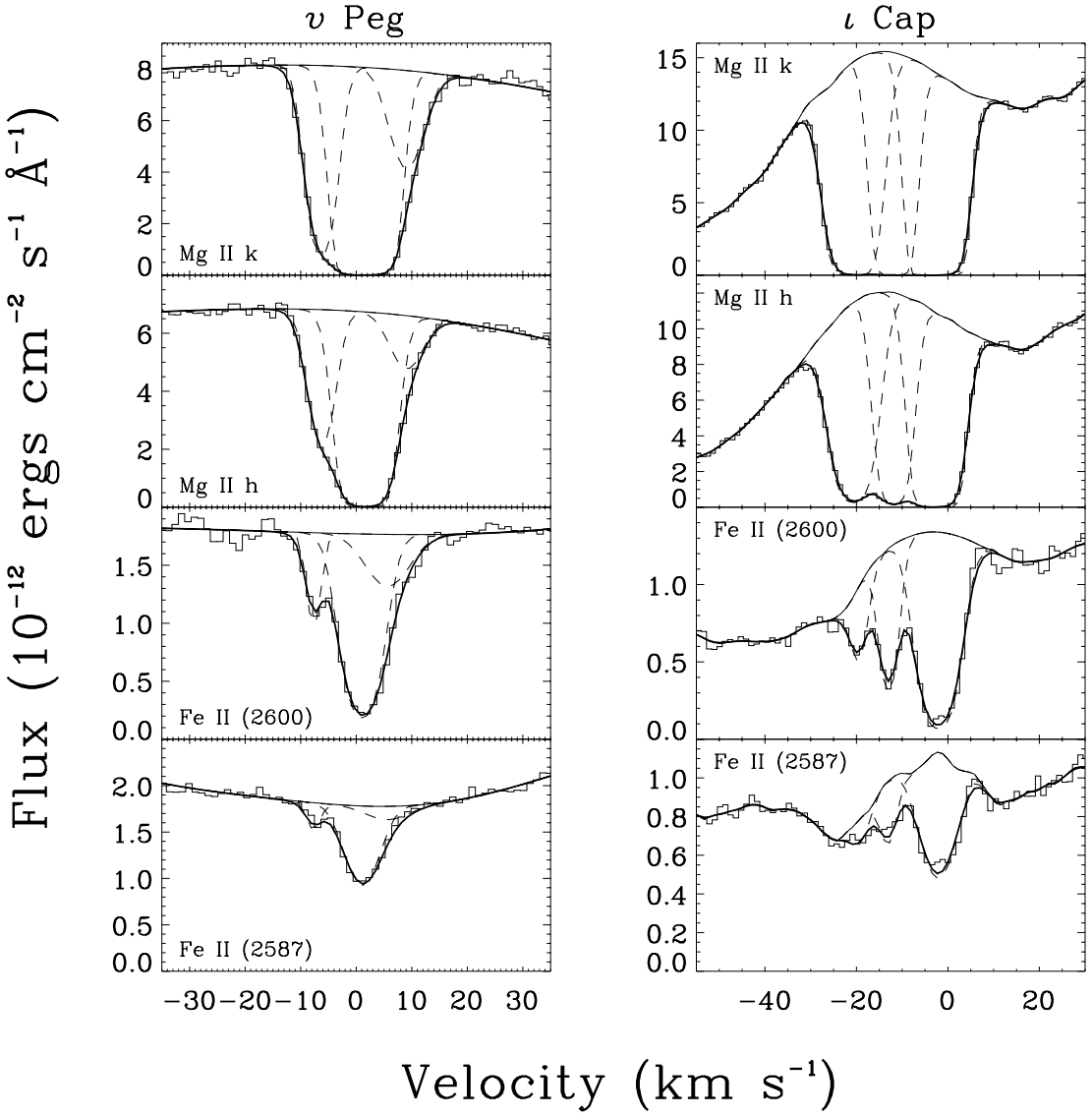

FIG. 1.—*Continued*

properties of nearby interstellar gas traced by the heavy ions: Mg II, Ca II, and Fe II.

3.1. *Velocity Distribution*

The kinematics of the LISM has been studied in several papers (Crutcher 1982; Lallement & Bertin 1992; Lallement et al. 1995; Frisch 1995; Vallerga et al. 1993). If we assume that each warm cloudlet structure in the LISM is moving with a single-valued bulk velocity, then we can calculate a unique velocity vector for each individual cloud. Because of the small number of lines of sight previously studied, and because solving for a single velocity vector requires a correlation of velocities across a large region of the sky, unique velocity vectors have only been calculated for the two nearest clouds with the largest angular size: the LIC and the G Cloud (Lallement et al. 1995). In the heliocentric rest frame, the LIC, in which the Sun is embedded, is flowing toward Galactic coordinates $l = 186°$ and $b = -16°$ at a speed of 25.7 ± 0.5 km s^{-1} (Witte et al. 1993; Lallement & Bertin 1992). The G Cloud has a very similar velocity vector, flowing toward Galactic coordinates $l = 184.°5$ and $b = -20.°5$ at a speed of 29 km s^{-1} (Lallement et al. 1995). Using these vectors we compute the projected LIC and G velocities for all stars in Tables 1 and 5. This compilation contains more than a factor of 10 more lines of sight than were originally used for the initial estimates of the velocity vectors of the LIC and G clouds. A detailed analysis of the spatial correlation of velocities into cloud structures will be presented in a future paper.

Figure 3 shows the distribution of velocities, with respect to the local standard of rest (LSR). Because we limit our target list to those located within 100 pc, we can neglect the effect of differential Galactic rotation. We convert from heliocentric velocities to the LSR frame using the Dehnen & Binney (1998) analysis of *Hipparcos* stellar kinematics. The velocity distributions of Fe II, Ca II, and Mg II absorption are all similar, with 94% of all velocity components within 20 km s^{-1} of the LSR. The particular shape of the distribution profiles is determined by the nonrandom selection of observed targets. For example, the large number of components at $V_{\rm LSR} \sim 10$ km s^{-1} in the Mg II distribution is domi-

TABLE 3

FIT PARAMETERS FOR Mg II LISM COMPONENTS WITHIN 100 pc

HD Number	Other Name	Component Number	v (km s^{-1})	b (km s^{-1})	log $N_{\rm Mg\,II}$ log (cm^{-2})	Reference
128620	α Cen A	1	-18.0 ± 0.2	2.27 ± 0.08	12.74 ± 0.06	1
		1	-17.7 ± 1.5	2.19	12.71	2
		1	-17.8 ± 0.1	2.26 ± 0.02	12.691 ± 0.003	1 of 2
128621	α Cen B	1	-18.1 ± 0.1	2.34 ± 0.21	12.73 ± 0.11	1
48915	Sirius	1	18.7 ± 1.1	2.71 ± 0.11	12.22 ± 0.04	3
		2	13.1 ± 1.1	3.08 ± 0.28	11.95 ± 0.06	3
22049	ϵ Eri	1	20.61 ± 0.25	2.81 ± 0.48	12.56 ± 0.05	4
201091	61 Cyg A	1	-3.0 ± 2.0	3.0 ± 0.4	12.4 ± 0.2	5
		2	-9.0 ± 1.0	3.0 ± 0.4	13.0 ± 0.2	5
61421	Procyon	1	20.80 ± 0.63	2.30 ± 0.07	12.36 ± 0.02	6
		2	23.37 ± 0.95	2.30 ± 0.07	12.11 ± 0.02	6
26965	40 Eri A	1	21.8 ± 1.0	2.4 ± 0.2	12.47 ± 0.03	5
165341	70 Oph	1	-26.64 ± 0.21	3.09 ± 0.27	13.51 ± 0.17	4
		2	-32.91 ± 1.51	3.43 ± 0.91	12.14 ± 0.22	4
		3	-43.36 ± 0.21	2.76 ± 0.15	12.04 ± 0.05	4
187642	α Aql	1	-17.9 ± 1.5	2.62	12.76	2
		2	-21.5 ± 1.5	2.86	12.76	2
		3	-25.3 ± 1.5	3.09	12.61	2
155886	36 Oph A	1	-27.9 ± 0.2	3.15 ± 0.25	13.05 ± 0.15	7
131156A...	ξ Boo A	1	-17.15 ± 0.25	2.54 ± 0.09	12.48 ± 0.04	4
39587	χ^1 Ori	1	23.35 ± 0.10	3.25 ± 0.06	12.58 ± 0.02	4
20630	κ^1 Cet	1	20.78 ± 0.13	3.26 ± 0.15	12.34 ± 0.02	4
		2	13.33 ± 0.05	2.68 ± 0.09	12.21 ± 0.02	4
		3	7.25 ± 0.34	2.48 ± 0.38	11.42 ± 0.05	4
197481	AU Mic	1	-21.22 ± 0.19	4.94 ± 0.74	13.20 ± 0.17	4
62059	β Gem	1	33.4 ± 0.6	2.49 ± 0.21	12.15 ± 0.03	8
		2	22.2 ± 0.6	3.18 ± 0.43	12.53 ± 0.04	8
124897	α Boo	1	-13.93 ± 0.14	2.68 ± 0.19	12.599 ± 0.009	4
33262	ζ Dor	1	14.12 ± 0.37	5.76 ± 0.37	13.01 ± 0.07	4
		2	8.45 ± 0.23	3.30 ± 0.19	13.23 ± 0.08	4
34029	α Aur	1	22.0 ± 1.0	2.53 ± 0.11	12.83 ± 0.02	6
		1	22.9 ± 1.5	2.58	12.81	9
36705	AB Dor	1	19.6 ± 0.7	2.8 ± 0.5	12.7 ± 0.2	10
		2	14.5 ± 0.8	3.0 ± 0.8	12.8 ± 0.4	10
		3	5.2 ± 0.1	3.8 ± 0.1	13.13 ± 0.06	10
128167	σ Boo	1	-2.28 ± 0.44	1.83 ± 0.41	11.23 ± 0.10	4
		2	-12.86 ± 0.21	2.68 ± 0.04	12.69 ± 0.02	4
432.....	β Cas	1	9.9 ± 0.4	2.55 ± 0.25	12.44 ± 0.08	8
23754	τ^6 Eri	1	41.40 ± 0.93	2.55 ± 1.10	11.51 ± 0.16	4
		2	27.94 ± 0.14	3.06 ± 0.73	13.84 ± 0.93	4
		3	17.02 ± 0.27	3.89 ± 0.26	13.01 ± 0.08	4
		4	8.82 ± 0.20	2.43 ± 0.20	12.15 ± 0.05	4
11443	α Tri	1	18.4 ± 0.4	0.80 ± 0.99	12.20 ± 0.07	8
		2	14.2 ± 0.3	4.07 ± 0.99	12.76 ± 0.07	8
29139	α Tau	1	51.81 ± 0.03	3.17 ± 0.10	12.20 ± 0.03	4
22468	HR 1099	1	21.9 ± 0.06	2.61 ± 0.09	12.12 ± 0.01	11
		2	14.8 ± 0.07	2.42 ± 0.08	11.74 ± 0.02	11
		3	8.2 ± 0.10	3.19 ± 0.10	11.49 ± 0.08	11
4128	β Cet	1	9.1 ± 0.1	2.46 ± 0.08	14.245 ± 0.104	11
		2	1.6 ± 0.1	3.71 ± 0.10	12.668 ± 0.020	11
		1	9.1	2.46	14.245	11
		2	3.4 ± 0.3	2.46	12.425 ± 0.026	11
		3	-0.4 ± 0.1	2.46	12.326 ± 0.031	11
8538	δ Cas	1	13.0 ± 1.5	2.97	12.76	12
		1	13.1 ± 1.5	2.86	12.83	2
120315	η UMa	1	3.17 ± 1.56	5.91 ± 3.77	11.30 ± 0.12	4 (see 13)
		2	-2.06 ± 0.12	2.53 ± 0.21	12.64 ± 0.02	4 (see 13)
209952	α Gru	1	-23.49 ± 0.43	3.69 ± 0.36	11.71 ± 0.07	4
		2	-14.69 ± 0.29	3.11 ± 0.28	13.79 ± 0.22	4
		3	-7.45 ± 0.23	2.39 ± 0.34	12.87 ± 0.16	4
155555	V824 Ara		-30 to -8		$\geq$13.3	4
	HZ 43	1	-5.33 ± 0.78	2.99 ± 0.48	12.41 ± 0.14	4
82210	DK UMa	1	9.63 ± 0.04	2.52 ± 0.10	12.61 ± 0.01	4
62044	σ Gem	1	32.3 ± 0.4	2.17 ± 0.25	12.06 ± 0.03	8

TABLE 3—*Continued*

HD Number	Other Name	Component Number	v (km s^{-1})	b (km s^{-1})	log $N_{\rm Mg\,II}$ log (cm^{-2})	Reference
		2	21.8 ± 0.3	3.46 ± 0.25	12.52 ± 0.03	8
215789	ϵ Gru	1	12.2 ± 1.5	4.7	12.53	14
		2	6.8 ± 1.5	5.0	12.38	14
		3	-1.7 ± 1.5	2.6	14.49	14
		4	-7.3 ± 1.5	2.0	13.95	14
		5	-12.3 ± 1.5	4.4	13.04	14
		6	-22.4 ± 1.5	3.0	12.20	14
27808	SAO 76593	1	23.1 ± 0.4	3.4 ± 0.4	12.86 ± 0.11	15
28568	SAO 93981	1	23.9 ± 0.5	3.3 ± 0.7	12.59 ± 0.15	15
		2	16.5 ± 1.6	2.5 ± 1.6	11.93 ± 0.27	15
26345	SAO 93801	1	21.1 ± 0.5	3.8 ± 0.7	12.65 ± 0.08	15
		2	13.6 ± 1.1	1.9 ± 1.3	11.94 ± 0.29	15
28736	SAO 111879	1	21.6 ± 0.5	4.4 ± 0.6	12.65 ± 0.05	15
		2	13.4 ± 0.7	1.7 ± 0.9	12.06 ± 0.25	15
		3	-4.3 ± 0.4	2.4 ± 0.6	12.25 ± 0.15	15
31845	101 Tau	1	22.4 ± 0.3	3.7 ± 0.5	12.49 ± 0.05	15
29225	SAO 94033	1	22.5 ± 0.2	3.7 ± 0.3	12.68 ± 0.04	15
28608	SAO 93982	1	23.2 ± 0.4	3.1 ± 0.4	12.42 ± 0.06	15
		2	15.8 ± 0.9	3.1 ± 0.4	12.18 ± 0.08	15
29419	SAO 76683	1	23.2 ± 0.2	3.1 ± 0.3	12.69 ± 0.08	15
		2	12.3 ± 0.2	2.1 ± 1.2	12.66 ± 0.33	15
164058	γ Dra		-20 to -5		$\geq$13.6	4
28205	V993 Tau	1	23.3 ± 0.3	2.3 ± 0.6	12.59 ± 0.28	15
		2	14.8 ± 1.7	4.2 ± 1.6	12.06 ± 0.14	15
28406	SAO 93963	1	22.1 ± 0.3	4.3 ± 0.3	12.67 ± 0.07	15
28033	SAO 76609	1	23.6 ± 0.5	3.2 ± 0.8	12.89 ± 0.35	15
28237	SAO 93945	1	22.4 ± 0.7	3.9 ± 0.9	12.42 ± 0.12	15
		2	15.6 ± 1.9	4.0 ± 1.9	12.17 ± 0.20	15
26784	SAO 93831	1	23.0 ± 1.0	2.9 ± 0.6	12.32 ± 0.13	15
		2	15.5 ± 1.1	3.7 ± 1.2	12.34 ± 0.12	15
21847	SAO 56530	1	21.1 ± 0.3	2.7 ± 1.0	13.14 ± 0.37	15
28483	SAO 93973	1	20.8 ± 0.3	3.8 ± 0.5	12.67 ± 0.15	15
27561	SAO 93885	1	22.2 ± 0.5	4.1 ± 0.7	12.50 ± 0.06	15
		2	14.4 ± 0.8	2.5 ± 1.0	12.04 ± 0.19	15
30738	SAO 93973	1	20.3 ± 0.4	3.8 ± 0.5	12.48 ± 0.10	15
220657	υ Peg	1	9.90 ± 0.97	3.56 ± 0.55	11.88 ± 0.15	4
		2	1.73 ± 0.13	4.07 ± 0.23	13.44 ± 0.07	4
		3	-6.59 ± 0.59	2.78 ± 0.26	12.38 ± 0.07	4
27848	SAO 93913	1	22.4 ± 1.0	3.8 ± 1.2	12.56 ± 0.24	15
		2	16.4 ± 2.2	2.7 ± 1.6	11.88 ± 0.31	15
203387	ι Cap	1	-20.57 ± 0.28	4.76 ± 0.16	13.17 ± 0.06	4
		2	-11.87 ± 0.20	3.27 ± 0.74	13.23 ± 0.26	4
		3	-2.35 ± 0.16	4.04 ± 0.08	13.61 ± 0.03	4
	G191-B2B	1	20.6 ± 2.0	2.7	12.63	16
		2	9.9 ± 2.0	3.5	13.28	16
		3	-1.7 ± 2.0	2.0	11.00	16
		1	20.6 ± 1.5	2.6	12.72	2
		2	9.9 ± 1.5	3.3	13.59	2
		3	-1.7 ± 1.5	1.9	10.97	2
111812	31 Com	1	-3.5 ± 0.1	2.39 ± 0.10	12.514 ± 0.010	11
		1	-3.3 ± 0.5	2.36 ± 0.11	12.50 ± 0.03	8

NOTE.— Table 3 is also available in machine-readable form in the electronic edition of the *Astrophysical Journal Supplement*.

REFERENCES.—(1) Linsky & Wood 1996; (2) Lallement et al. 1995; (3) Lallement et al. 1994; (4) this paper; (5) Wood & Linsky 1998; (6) Linsky et al. 1995; (7) Wood, Linsky, & Zank 2000; (8) Dring et al. 1997; (9) Linsky et al. 1993; (10) Brandt et al. 2001; (11) Piskunov et al. 1997; (12) Lallement & Ferlet 1997; (13) Frisch et al. 1999; (14) Lecavelier des Etangs et al. 1997; (15) Redfield & Linsky 2001; (16) Lemoine et al. 1996.

nated by the LIC component for the lines of sight to the 18 stars in the Hyades sample (*shaded*), all of which have nearly identical velocities (Redfield & Linsky 2001). The spatial correlation of velocities into cloud structures will therefore influence the shape of these distribution profiles. The mean velocity for the Fe II distribution is $\langle v_{\rm LSR}({\rm Fe\ II})\rangle \sim -0.4$ km s^{-1} with a standard deviation of $\langle v^2_{\rm LSR}({\rm Fe\ II})\rangle^{1/2} \sim 10.6$ km s^{-1}. We find similar values for Ca II and Mg II: $\langle v_{\rm LSR}({\rm Ca\ II})\rangle \sim -3.4$ km s^{-1} and $\langle v^2_{\rm LSR}({\rm Ca\ II})\rangle^{1/2} \sim 9.8$ km s^{-1}, $\langle v_{\rm LSR}({\rm Mg\ II})\rangle \sim 2.4$ km s^{-1} and $\langle v^2_{\rm LSR}({\rm Mg\ II})\rangle^{1/2} \sim 11.2$ km s^{-1}. These values agree with the Ca II optical surveys by Vallerga et al. (1993) and Welty

TABLE 4

FIT PARAMETERS FOR Fe II LISM COMPONENTS WITHIN 100 pc

HD Number	Other Name	Component Number	v (km s^{-1})	b (km s^{-1})	log $N_{\rm Fe\,II}$ log (cm^{-2})	Reference
128620	α Cen A	1	-17.7 ± 0.1	1.78 ± 0.14	12.455 ± 0.022	1
		1	-18.3 ± 1.5	1.34	12.36	2
		1	-18.2 ± 0.1	1.43 ± 0.02	12.441 ± 0.004	1 of 2
128621	α Cen B	1	-17.77 ± 0.44	2.17 ± 0.69	12.50 ± 0.13	3
48915	Sirius	1	20.1 ± 1.1	2.05 ± 0.28	11.93 ± 0.03	4
		2	14.4 ± 1.1	3.00 ± 0.20	11.73 ± 0.15	4
22049	ϵ Eri	1	21.3 ± 0.3	2.54 ± 0.70	12.36 ± 0.07	5
		1	19.51 ± 0.98	2.73 ± 0.36	12.12 ± 0.16	3
61421	Procyon	1	20.23 ± 0.10	2.71 ± 0.13	12.27 ± 0.02	6
165341	70 Oph	1	-26.48 ± 0.08	3.92 ± 0.13	12.83 ± 0.03	3
187642	α Aql	1	-17.6 ± 1.5	1.97	12.49	2
		2	-20.5 ± 1.5	2.09	12.41	2
		3	-24.2 ± 1.5	2.42	12.30	2
155886	36 Oph A	1	-28.4 ± 0.4	2.12 ± 0.61	12.65 ± 0.25	7
216956	α PsA	1	-3.2 ± 1.5	2.7	12.58	8
		2	-9.7 ± 1.5	2.8	12.26	2
		2	-16.0 ± 1.5	1.53	12.84	2
		3	-18.3 ± 1.5	1.83	12.81	2
39587	χ^1 Ori	1	23.38 ± 0.23	2.23 ± 0.37	12.21 ± 0.04	3
20630	κ^1 Cet	1	14.80 ± 1.14	3.14 ± 1.36	11.63 ± 0.18	3
		2	20.97 ± 0.43	2.63 ± 0.66	11.93 ± 0.09	3
62059	β Gem	1	31.52 ± 0.17	2.80 ± 0.28	11.97 ± 0.03	3
		2	19.36 ± 0.11	2.31 ± 0.18	12.23 ± 0.03	3
102647	β Leo	1	11.80 ± 0.22	0.73 ± 0.29	12.60 ± 0.28	3
		2	0.50 ± 0.14	2.36 ± 0.27	12.36 ± 0.04	3
124897	α Boo	1	-13.94 ± 0.13	1.75 ± 0.18	12.24 ± 0.02	3
33262	ζ Dor	1	12.52 ± 1.35	6.01 ± 0.65	12.78 ± 0.04	3
		2	7.36 ± 0.92	2.22 ± 1.08	12.68 ± 0.17	3
34029	α Aur	1	20.65 ± 0.10	2.36 ± 0.12	12.49 ± 0.02	6
		1	20.68 ± 1.5	2.40	12.48	9
128167	σ Boo	1	-2.85 ± 0.42	1.67 ± 1.05	11.82 ± 0.14	3
		2	-13.16 ± 0.57	2.00 ± 0.19	12.37 ± 0.04	3
432	β Cas	1	9.5 ± 0.3	1.78 ± 0.8	12.36 ± 0.1	5
23754	τ^6 Eri	1	27.06 ± 1.22	3.24 ± 0.21	12.73 ± 0.07	3
		2	15.84 ± 1.64	4.03 ± 1.24	12.71 ± 0.12	3
39060	β Pic	1	10.1 ± 1.5	2.3	12.95	2
		1	10.12 ± 0.18	1.88 ± 0.27	13.15 ± 0.36	3
11443	α Tri	1	17.6 ± 0.5	1.52 ± 1.0	12.40 ± 0.2	5
		2	12.7 ± 0.5	1.17 ± 1.0	12.29 ± 0.2	5
22468	HR 1099		...	...	$\leq$12.2	3
120315	η UMa	1	-2.65 ± 0.65	2.11 ± 0.01	12.406 ± 0.002	3 (see 10)
209952	α Gru	1	-22.30 ± 1.89	3.07 ± 0.38	11.25 ± 0.04	3
		2	-12.72 ± 0.75	2.23 ± 0.25	12.98 ± 0.11	3
		3	-8.44 ± 0.76	4.14 ± 0.72	13.06 ± 0.13	3
	HZ 43	1	-5.00 ± 0.37	1.96 ± 0.74	11.99 ± 0.10	3
82210	DK UMa	1	9.57 ± 0.18	2.07 ± 0.29	12.30 ± 0.04	3
80007	β Car	1	-4.23 ± 0.76	1.01 ± 0.28	12.45 ± 0.07	3
		2	3.51 ± 0.59	2.30 ± 0.46	13.76 ± 0.17	3
215789	ϵ Gru	1	12.2 ± 1.5	...	11.45	11
		2	6.8 ± 1.5	...	12.32	11
		3	-1.7 ± 1.5	...	12.85	11
		4	-7.3 ± 1.5	...	12.86	11
		5	-12.3 ± 1.5	...	12.95	11
		6	-22.4 ± 1.5	...	11.91	11
220657	υ Peg	1	7.00 ± 2.64	3.44 ± 2.58	12.00 ± 0.38	3
		2	1.13 ± 0.41	3.99 ± 0.35	13.00 ± 0.03	3
		3	-7.61 ± 0.18	1.57 ± 0.27	12.01 ± 0.06	3
203387	ι Cap	1	-19.35 ± 1.44	3.81 ± 1.68	12.34 ± 0.14	3
		2	-12.67 ± 0.40	2.53 ± 0.34	12.52 ± 0.13	3
		3	-2.17 ± 0.10	4.71 ± 0.24	13.180 ± 0.008	3
	G191-B2B	1	20.6 ± 2.0	2.2	12.48	12
		2	9.9 ± 2.0	3.0	12.95	12
		3	-1.7 ± 2.0	1.7	11.00	12
111812	31 Com	1	-2.4 ± 0.3	0.71 ± 0.4	12.55 ± 0.1	5

NOTE.— Table 4 is also available in machine-readable form in the electronic edition of the *Astrophysical Journal Supplement*.

REFERENCES.—(1) Linsky & Wood 1996; (2) Lallement et al. 1995; (3) this paper; (4) Lallement et al. 1994; (5) Dring et al. 1997; (6) Linsky et al. 1995; (7) Wood et al. 2000; (8) Ferlet et al. 1995; (9) Linsky et al. 1993; (10) Frisch et al. 1999; (11) Lecavelier des Etangs et al. 1997; (12) Lemoine et al. 1996.

TABLE 5

PARAMETERS FOR STARS WITHIN 100 pc WITH Ca II HIGH-RESOLUTION SPECTRA

HD Number	Other Name	Spectral Type	m_V	v_R (km s^{-1})	l (deg)	b (deg)	Distance[a] (pc)	v_{LIC}[b] (km s^{-1})	v_G[c] (km s^{-1})
128620	α Cen A	G2 V	−0.0	−24.6	315.7	−0.7	1.3	−15.6	−18.0
187642	α Aql	A7 V	0.8	−26.1	47.7	−8.9	5.1	−17.1	−18.2
216956	α PsA	A3 V	1.2	6.5	20.5	−64.9	7.7	−3.6	−1.9
159561	α Oph	A5 III	2.1	12.6	35.9	22.6	14.3	−22.5	−25.7
203280	α Cep	A7 IV	2.4	−10	101.0	9.2	15.0	0.9	1.4
115892	ι Cen	A2 V	2.7	0.1	309.4	25.8	18.0	−15.3	−18.7
12311	α Hyi	F0 V	2.9	7	289.5	−53.8	21.9	2.5	4.1
87901	α Leo	B7 V	1.4	5.9	226.4	48.9	23.8	6.9	5.7
156164	δ Her	A3 IV	3.1	−40.0	46.8	31.4	24.1	−19.7	−22.7
74956	δ Vel	A1 V	2.0	2.2	272.1	−7.4	24.4	2.6	2.5
16970	γ Cet	A3 V	3.5	−5.1	168.9	−49.4	25.1	20.8	25.1
177724	ζ Aql	A0 V	3.0	−25	46.9	3.3	25.5	−19.1	−20.9
18978	τ^3 Eri	A4 V	4.1	−9.8	213.5	−60.3	26.4	17.1	20.9
108767	δ Crv	B9.5 V	3.0	9	295.5	46.0	26.9	−10.9	−14.3
19356	β Per	B8 V	2.1	4.0	149.0	−14.9	28.5	20.9	24.3
161868	γ Oph	A0 V	3.8	−7	28.0	15.4	29.1	−24.0	−27.1
210418	θ Peg	A2 V	3.5	−6	67.4	−38.7	29.6	−4.7	−3.4
358	α And	B8 IV	2.1	−11.7	111.7	−32.8	29.8	9.5	12.4
8538	δ Cas	A5 III–IV	2.7	6.7	127.2	−2.4	30.5	13.0	15.3
120315	η UMa	B3 V	1.9	−10.9	100.7	65.3	30.9	−5.8	−8.1
209952	α Gru	B7 IV	1.7	11.8	350.0	−52.5	31.1	−8.7	−8.1
213558	α Lac	A1 V	3.8	−4.0	101.3	−6.6	31.4	3.1	4.4
88955	HR 4023	A2 V	3.8	7.4	274.3	11.9	31.5	−0.7	−2.0
112413	α^2 CVn	A0	2.9	−3.3	118.3	78.8	33.8	−5.3	−7.9
177756	λ Aql	B9 V	3.4	−12	30.3	−5.5	38.4	−23.1	−25.4
44769	HR 2298	A5 IV	4.4	14.6	205.7	−4.0	39.4	23.7	26.3
79469	θ Hya	B9.5 V	3.9	−10	228.8	32.5	39.5	11.4	11.1
215789	ϵ Gru	A3 V	3.5	0	338.3	−56.5	39.7	−6.0	−5.1
35497	β Tau	B7 III	1.7	9.2	178.0	−3.8	40.2	24.8	28.0
218045	α Peg	B9 III	2.5	−3.5	88.3	−40.4	42.8	2.2	4.4
10144	α Eri	B3 V	0.5	16	290.8	−58.8	44.1	3.0	4.8
212061	γ Aqr	A0 V	3.8	−15	62.2	−45.8	48.4	−4.4	−2.9
106625	γ Crv	B8 III	2.6	−4.2	291.0	44.5	50.6	−9.6	−12.8
222439	κ And	B9 IV	4.1	−9	109.8	−16.7	52.0	7.7	9.9
58715	β CMi	B8 V	2.9	22	209.5	11.7	52.2	20.7	22.4
186882	δ Cyg	B9.5 IV	2.9	−20.1	78.7	10.2	52.4	−8.5	−9.2
193924	α Pav	B2 IV	1.9	2.0	340.9	−35.2	56.2	−14.0	−14.7
213998	η Aqr	B9 IV–V	4.0	−8	66.8	−47.6	56.3	−2.8	−1.0
129685	c^2 Cen	A0 V	4.9	−5.0	327.7	22.2	63.5	−20.6	−24.3
214923	ζ Peg	B8 V	3.4	7	78.9	−40.7	64.1	−0.8	1.1
98664	σ Leo	B9.5 V	4.0	−5.3	253.4	59.9	65.6	−1.5	−3.9
32630	η Aur	B3 V	3.2	7.3	165.4	0.3	67.2	23.0	26.0
45320	HR 2324	A3 V	5.9	10	211.5	−6.2	70.1	22.9	25.5
152614	ι Oph	B8 V	4.4	−21	28.7	30.7	71.7	−23.3	−26.9
196867	α Del	B9 IV	3.8	−3.4	60.3	−15.3	73.8	−12.0	−12.2
35468	γ Ori	B2 III	1.6	18.2	196.9	−16.0	74.5	25.3	28.7
116658	α Vir	B1 III–IV	1.0	1.0	316.1	50.8	80.4	−15.6	−19.5
97277	β Crt	A1 V	4.5	6.4[d]	274.8	34.5	81.6	−3.6	−6.0
191692	θ Aql	B9.5 III	3.2	−27.3	41.6	−18.1	88.0	−16.8	−17.7
127972	η Cen	B1.5 V	2.3	−0.2	322.8	16.7	94.6	−19.3	−22.6
138749	θ CrB	B6 V	4.2	−25	49.7	54.7	95.3	−16.2	−19.6
147394	τ Her	B5 IV	3.9	−13.8	72.5	45.0	96.4	−12.1	−14.6
141569	...	B9	7.0	−6.4[e]	4.2	36.9	99.0	−24.1	−28.2

[a] *Hipparcos* distances (Perryman et al. 1997).
[b] Predicted projected LIC velocity from Lallement & Bertin 1992.
[c] Predicted projected G velocity from Lallement & Bertin 1992.
[d] Duflot et al. 1995.
[e] Frisch 1987.

et al. (1996). The most extreme point at $v_{LSR} \sim 40$ km s^{-1} corresponds to the line of sight toward α Tau, providing additional support to the claim that the absorption is in fact circumstellar and not LISM absorption (see § 2.2).

If Mg II, Fe II, and Ca II are all similarly distributed in the LISM, we would expect to see absorption at the same velocity in all three ions, along a particular line of sight. Of the 63 individual lines of sight, with UV observations, listed in

TABLE 6

FIT PARAMETERS FOR Ca II LISM COMPONENTS WITHIN 100 pc

HD Number	Other Name	Component Number	v (km s^{-1})	b (km s^{-1})	log $N_{\rm Ca\,II}$ log (cm^{-2})	Reference
128620	α Cen A		...	...	$\leq$9.70	1
187642	α Aql	1	-25.2 ± 0.2	1.5 ± 0.4	$9.60^{+0.08}_{-0.10}$	2
		2	-18.7 ± 0.2	3.6 ± 0.4	10.16 ± 0.03	2
		1	-26.0 ± 1.0	1.4 ± 0.4	$9.48^{+0.11}_{-0.15}$	3
		2	-21.4 ± 1.0	2.0 ± 1.2	$9.86^{+0.20}_{-0.40}$	3
		3	-17.4 ± 1.0	2.0 ± 0.6	$9.86^{+0.11}_{-0.15}$	3
216956	α PsA	1	-1.8	...	9.72	4
159561	α Oph	1	-33.0 ± 0.3	2.37 ± 0.47	10.43 ± 0.05	5
		2	-26.3 ± 0.3	2.73 ± 0.55	$11.46^{+0.08}_{-0.10}$	5
		3	-22.2 ± 0.3	1.21 ± 0.24	$10.38^{+0.05}_{-0.06}$	5
		1	-32.0 ± 0.5	$1.5^{+1.0}_{-0.5}$	10.20 ± 0.20	6
		2	-28.4 ± 0.3	1.4 ± 0.2	$10.80^{+0.15}_{-0.20}$	6
		3	-26.2 ± 0.2	1.5 ± 0.3	$11.20^{+0.13}_{-0.15}$	6
		4	-23.6 ± 0.5	$2.0^{+0.3}_{-0.5}$	$11.00^{+0.10}_{-0.20}$	6
		1	-31.0	...	10.01	4
		2	-25.3	...	11.40	4
203280	α Cep	1	0.2 ± 1.0	1.7 ± 0.3	$9.85^{+0.15}_{-0.24}$	7
115892	ι Cen	1	-18.2 ± 0.1	2.2 ± 0.2	$10.40^{+0.05}_{-0.04}$	8
		1	-17.7	...	10.38	4
12311	α Hyi	1	4.9 ± 0.1	$2.3^{+0.2}_{-0.8}$	$10.70^{+0.08}_{-0.16}$	8
		2	9.8 ± 0.4	$3.2^{+0.8}_{-1.0}$	$10.46^{+0.14}_{-0.16}$	8
		1	4.0	2.0	$10.66^{+0.12}_{-0.17}$	9
		2	8.0	2.0	$10.30^{+0.10}_{-0.12}$	9
		1	5.1	...	...	4
		2	10.8	...	10.01	4
87901	α Leo		...	...	$\leq$9.62	10
156164	δ Her	1	-19.5 ± 1.0	2.3 ± 0.5	$10.49^{+0.06}_{-0.08}$	7
		1	-28.7	...	9.18	4
		2	-19.2	...	10.47	4
74956	δ Vel	1	1.3 ± 0.4	4.2 ± 0.5	10.38 ± 0.04	2
		2	11.8 ± 0.3	3.7 ± 0.4	10.64 ± 0.02	2
		3	15.6 ± 0.1	1.1 ± 0.3	$9.93^{+0.08}_{-0.10}$	2
		1	2.5	...	9.85	4
		2	7.7	...	...	4
		3	13.3	...	10.59	4
16970	γ Cet		...	...	$\leq$9.56	2
177724	ζ Aql	1	$-30.2^{+0.5}_{-0.4}$	$3.50^{+0.98}_{-0.72}$	$10.18^{+0.07}_{-0.08}$	10
		2	-21.3 ± 0.6	$5.40^{+1.21}_{-0.96}$	$10.30^{+0.06}_{-0.08}$	10
		1	-29.3	...	10.13	4
		2	-22.1	...	...	4
18978	τ^3 Eri	1	15.9 ± 1.0	2.7	$10.30^{+0.18}_{-0.30}$	9
		2	20.9 ± 1.0	1.1	$10.48^{+0.12}_{-0.18}$	9
108767	δ Crv	1	-0.5 ± 0.3	1.25 ± 0.25	10.53 ± 0.04	5
19356	β Per		...	...	$\leq$9.48	10
161868	γ Oph	1	-33.0 ± 1.0	3.0 ± 1.0	$10.48^{+0.12}_{-0.30}$	8
		2	-29.9 ± 0.3	2.0 ± 0.5	$10.62^{+0.16}_{-0.14}$	8
		1	-31.1 ± 1.0	3.3	$10.81^{+0.06}_{-0.07}$	9
210418	θ Peg	1	-4.2 ± 0.2	2.8 ± 0.3	$10.48^{+0.05}_{-0.06}$	2
358	α And	1	13.0 ± 0.8	3.6 ± 1.1	$10.30^{+0.10}_{-0.13}$	2
		1	8.9 ± 0.2	$3.9^{+0.50}_{-0.43}$	10.36 ± 0.04	10
8538	δ Cas	1	12.9 ± 1.5	0–1.5	$9.70^{+0.18}_{-0.30}$	7
		1	7.2	...	9.78	4
		2	11.6	...	9.92	4
120315	η UMa	1	-2.8 ± 0.3	$2.00^{+0.66}_{-0.56}$	$9.77^{+0.33}_{-0.66}$	10
209952	α Gru	1	-13.0 ± 0.5	1.8 ± 0.2	$10.30^{+0.05}_{-0.15}$	6
		2	-10.2 ± 1.0	2.3 ± 0.4	$10.05^{+0.20}_{-0.35}$	6
		1	-12.5	...	10.37	4
		2	-6.9	...	9.83	4
		3	-3.8	...	9.11	4
213558	α Lac	1	3.5 ± 1.0	1.6 ± 0.4	$10.00^{+0.11}_{-0.15}$	7
88955	HR 4023	1	-1.7 ± 0.2	2.5 ± 0.3	10.38 ± 0.05	2
		2	10.5 ± 0.1	2.0 ± 0.2	10.60 ± 0.03	2
		1	-4.5 ± 1.5	3.5	$10.36^{+0.09}_{-0.11}$	9
		2	9.3 ± 1.5	2.5	$10.66^{+0.09}_{-0.11}$	9

TABLE 6—*Continued*

HD Number	Other Name	Component Number	v (km s^{-1})	b (km s^{-1})	log $N_{\rm Ca\,II}$ log (cm^{-2})	Reference
		1	10.1	...	10.47	4
112413	α^2 CVn	1	-1.9 ± 0.2	$1.48^{+0.53}_{-0.36}$	$9.71^{+0.08}_{-0.07}$	10
177756	λ Aql		...	...	$\leq$9.58	10
44769	HR 2298	1	7 ± 1	...	$\geq$11.18	11
79469	θ Hya		...	...	$\leq$9.53	10
215789	ϵ Gru	1	-12.2 ± 0.2	$2.2^{+0.5}_{-0.4}$	$10.20^{+0.08}_{-0.12}$	8
		2	-7.2 ± 0.1	2.3 ± 0.5	$10.29^{+0.12}_{-0.18}$	8
		3	-1.1 ± 0.1	$2.7^{+0.3}_{-0.7}$	10.46 ± 0.08	8
		1	-13.0 ± 1.5	2.9	$10.28^{+0.06}_{-0.07}$	9
		2	-7.0 ± 1.5	2.6	$10.30^{+0.10}_{-0.12}$	9
		3	-1.1 ± 1.5	2.2	$10.28^{+0.06}_{-0.07}$	9
35497	β Tau		...	...	$\leq$9.32	10
218045	α Peg	1	-0.9 ± 0.3	$5.20^{+0.58}_{-0.50}$	10.53 ± 0.04	10
		1	-2.5 ± 1.0	2.5 ± 1.0	$10.20^{+0.21}_{-0.43}$	7
		2	-2.0 ± 1.5	1.9 ± 1.0	$10.20^{+0.21}_{-0.43}$	7
		3	5.5 ± 1.0	1.0431	0–9.78	7
		1	-3.3	...	...	4
		2	1.4	...	10.25	4
10144	α Eri	1	7.6 ± 0.4	$2.2^{+0.2}_{-0.3}$	$10.40^{+0.07}_{-0.10}$	6
		2	11.0 ± 0.4	$2.0^{+0.3}_{-0.2}$	$10.27^{+0.11}_{-0.09}$	6
		3	18.9 ± 0.4	$1.5^{+0.2}_{-0.5}$	$9.70^{+0.20}_{-0.30}$	6
		4	21.2 ± 0.4	$1.9^{+0.3}_{-0.4}$	$10.10^{+0.05}_{-0.20}$	6
		1	-4.4	...	...	4
		2	5.1	...	...	4
		3	9.1	...	10.60	4
		4	20.8	...	...	4
212061	γ Aqr	1	-4.5 ± 0.4	$1.2^{+0.6}_{-0.4}$	$9.90^{+0.10}_{-0.20}$	8
		1	-4.4 ± 0.7	$2.9^{+1.20}_{-0.86}$	$9.95^{+0.12}_{-0.18}$	10
		1	-4.6 ± 1.0	1.95 ± 0.2	$10.00^{+0.08}_{-0.10}$	7
106625	γ Crv	1	-2.0 ± 0.3	2.14 ± 0.43	$10.73^{+0.08}_{-0.10}$	5
		2	1.6 ± 0.3	1.71 ± 0.34	$10.18^{+0.08}_{-0.10}$	5
222439	κ And	1	$0.8^{+0.5}_{-0.4}$	$1.50^{+1.34}_{-0.72}$	$10.04^{+0.20}_{-0.08}$	10
		2	$7.6^{+0.7}_{-0.3}$	$6.30^{+0.54}_{-1.16}$	$10.79^{+0.03}_{-0.08}$	10
58715	β CMi		...	...	$\leq$9.70	10
186882	δ Cyg	1	-18.8 ± 0.3	0.47 ± 0.09	$10.45^{+0.04}_{-0.05}$	5
		2	-16.3 ± 0.3	2.99 ± 0.60	$10.46^{+0.04}_{-0.05}$	5
		3	-9.6 ± 0.3	2.55 ± 0.51	10.51 ± 0.04	5
193924	α Pav	1	-19.6 ± 0.1	0.8 ± 0.1	10.09 ± 0.03	2
		2	-18.6 ± 0.1	5.6 ± 0.1	11.02 ± 0.01	2
213998	η Aqr	1	-2.1 ± 0.3	$3.30^{+0.58}_{-0.49}$	10.43 ± 0.05	10
129685	c^2 Cen	1	-26.3 ± 0.2	1.2 ± 0.2	10.40 ± 0.15	12
		2	-16.9 ± 0.2	1.2 ± 0.2	10.67 ± 0.15	12
214923	ζ Peg	1	-2.2 ± 0.3	$3.70^{+0.55}_{-0.48}$	10.41 ± 0.05	10
98664	σ Leo		...	...	$\leq$9.51	10
32630	η Aur	1	6.8 ± 0.3	2.24 ± 0.44	$10.80^{+0.08}_{-0.10}$	5
		2	10.7 ± 0.3	1.51 ± 0.30	$10.83^{+0.08}_{-0.10}$	5
		3	17.8 ± 0.3	2.18 ± 0.44	10.54 ± 0.04	5
		1	6.8 ± 0.1	$2.30^{+0.16}_{-0.14}$	10.64 ± 0.02	10
		2	10.7 ± 0.1	1.70 ± 0.10	10.75 ± 0.01	10
		3	17.4 ± 0.1	$3.00^{+0.26}_{-0.22}$	10.56 ± 0.02	10
		1	7.0 ± 1.0	2.2 ± 0.5	$10.82^{+0.11}_{-0.16}$	7
		2	10.8 ± 1.0	1.5 ± 0.5	$10.86^{+0.11}_{-0.14}$	7
		3	17.7 ± 1.5	2.4 ± 2.0	$10.70^{+0.15}_{-0.22}$	7
		4	23.0 ± 1.5	1.9 ± 1.0	$9.78^{+0.12}_{-0.18}$	7
		1	6.4	...	...	4
		2	10.8	...	...	4
		3	18.5	...	10.67	4
45320	HR 2324	1	26 ± 1	...	$\geq$10.76	11
152614	ι Oph	1	-30.8 ± 0.4	$3.70^{+0.87}_{-0.71}$	$10.52^{+0.07}_{-0.08}$	10
		2	-21.5 ± 0.2	$2.60^{+0.35}_{-0.31}$	10.76 ± 0.04	10
		3	-11.0 ± 0.2	$4.00^{+0.45}_{-0.39}$	10.84 ± 0.04	10
196867	α Del	1	-14.0 ± 0.1	$1.78^{+0.30}_{-0.24}$	10.56 ± 0.03	10
		2	-10.4 ± 0.2	$0.42^{+1.00}_{-0.37}$	$10.04^{+0.09}_{-0.10}$	10
35468	γ Ori	1	16.0 ± 0.1	1.90 ± 0.20	$10.34^{+0.02}_{-0.04}$	10
		2	20.2 ± 0.1	$4.10^{+0.24}_{-0.18}$	10.70 ± 0.02	10

TABLE 6—*Continued*

HD Number	Other Name	Component Number	v (km s^{-1})	b (km s^{-1})	log $N_{\rm Ca\,II}$ log (cm^{-2})	Reference
		3	25.4 ± 0.1	$0.25^{+0.06}_{-0.04}$	10.79 ± 0.01	10
		4	27.8 ± 0.1	$1.40^{+0.23}_{-0.24}$	10.32 ± 0.03	10
116658	α Vir	1	-11.9 ± 0.3	3.29 ± 0.66	$10.46^{+0.04}_{-0.05}$	5
		2	-3.5 ± 0.3	1.28 ± 0.26	$10.46^{+0.04}_{-0.05}$	5
		1	-12.0 ± 0.1	$2.20^{+0.24}_{-0.21}$	10.26 ± 0.03	10
		2	-5.4 ± 0.4	$5.40^{+0.84}_{-0.59}$	$10.20^{+0.04}_{-0.05}$	10
		3	-3.7 ± 0.1	$0.61^{+0.22}_{-0.34}$	10.23 ± 0.02	10
		1	-11.1	...	...	4
		2	-3.2	...	10.43	4
97277	β Crt	1	1.4	...	10.84	4
		2	8.9	...	9.94	4
191692	θ Aql	1	-22.6 ± 0.1	$1.90^{+0.15}_{-0.13}$	10.72 ± 0.02	10
		2	-17.7 ± 0.1	$2.10^{+0.18}_{-0.21}$	$10.53^{+0.02}_{-0.03}$	10
127972	η Cen		...	...	≤ 9.70	12
138749	θ CrB	1	-19.9 ± 0.1	1.80 ± 0.14	10.69 ± 0.02	10
		2	-15.7 ± 0.1	$2.10^{+0.30}_{-0.27}$	10.41 ± 0.03	10
147394	τ Her	1	$-38.0^{+0.5}_{-0.3}$	$3.10^{+0.95}_{-0.64}$	10.40 ± 0.08	10
		2	$-33.5^{+0.3}_{-0.2}$	$0.60^{+1.08}_{-0.58}$	$10.04^{+0.10}_{-0.17}$	10
141569		1	-28.7 ± 1.5	4.5 ± 1.4	$11.45^{+0.11}_{-0.15}$	13
		2	-13.7 ± 1.5	4.45 ± 0.45	$11.23^{+0.04}_{-0.05}$	13

NOTE.— Table 6 is also available in machine-readable form in the electronic edition of the *Astrophysical Journal Supplement*.

REFERENCES.—(1) Crawford 1994; (2) Crawford, Lallement, & Welsh 1998; (3) Ferlet, Lallement, & Vidal-Madjar 1986; (4) Lallement, Vidal-Madjar, & Ferlet (1986); (5) Welty et al. 1996; (6) Crawford & Dunkin 1995; (7) Lallement & Bertin 1992; (8) Crawford, Craig, & Welsh 1997; (9) Bertin et al. 1993; (10) Vallerga et al. 1993; (11) Lagrange-Henri et al. 1991; (12) Centurion & Vladilo 1991; (13) Sahu et al. 1998.

Table 1, 27 have both Mg II and Fe II observations. Of the 53 individual lines of sight observed in the optical, and listed in Table 5, only seven have both optical Ca II and UV observations. Unfortunately, observational selection effects for the optical and UV lead to mutually exclusive sets of observed targets. Most UV targets are late-type stars with strong stellar emission lines over a faint continuum, while typical optical targets are early-type stars with few stellar

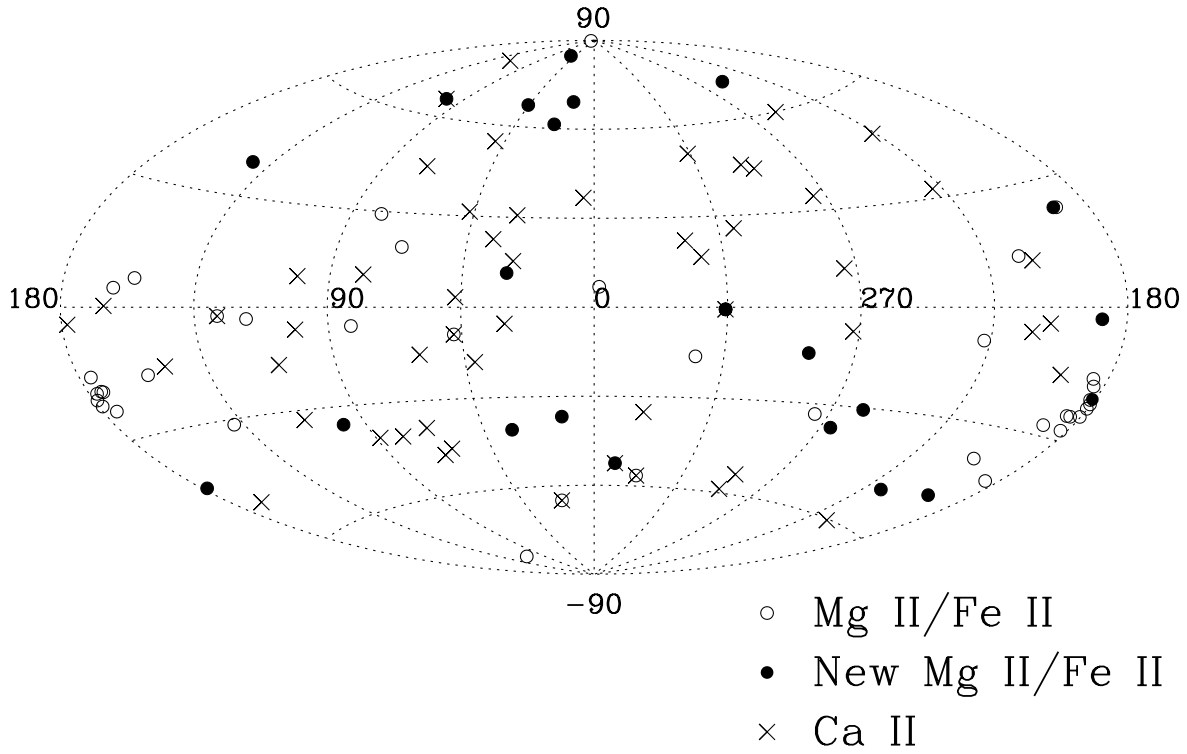

FIG. 2.—Location of all stars listed in Tables 1 and 5 are shown in Galactic coordinates. All *HST* targets with spectra of Mg II and Fe II are indicated by circles. Those stars with spectra analyzed in this work and shown in Fig. 1 are indicated by filled circles, while those previously analyzed and published are indicated by open circles. All Ca II targets listed in Table 5 are indicated by the symbol " ×."

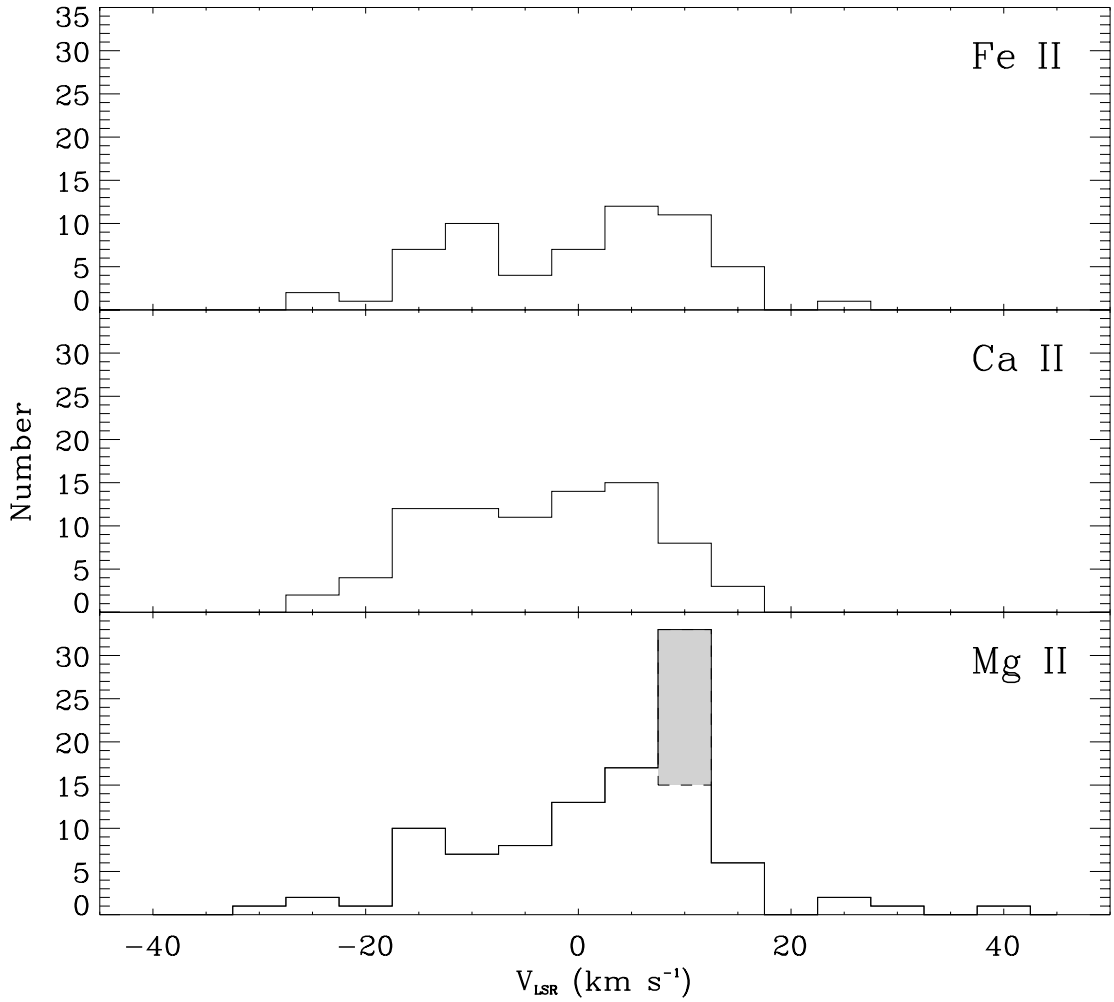

FIG. 3.—Distribution of velocity components, with respect to the local standard of rest (LSR). We convert from heliocentric velocities to the LSR frame using the Dehnen & Binney (1998) analysis of *Hipparcos* stellar kinematics. More than 94% of all velocity components lie within 20 km s^{-1} of the LSR. The bin size used is 5 km s^{-1}. The large number of components at $V_{LSR} \sim 10$ km s^{-1} in the Mg II distribution are dominated by the LIC component of the Hyades sample (Redfield & Linsky 2001). The 18 stars in this sample are indicated by the shaded region.

absorption lines over a strong continuum. In Figure 4, we show the distribution of velocity differences for the same components along a particular line of sight for different ions. The Mg II and Fe II comparison is most enlightening since we have a significantly larger sample to evaluate. The strong spike at zero velocity difference confirms the assumption that both ions are tracking the same collection of gas in the LISM. The mean velocity difference between Mg II and Fe II is $\langle v(\text{Mg II}) - v(\text{Fe II})\rangle \sim 0.3$ km s^{-1}, and the standard deviation is $\langle (v(\text{Mg II}) - v(\text{Fe II}))^2\rangle^{1/2} \sim 1.1$ km s^{-1}. While we have very few common velocity components between the optical Ca II and the UV ions Mg II and Fe II, the results are very similar: $\langle v(\text{Mg/Fe}) - v(\text{Ca II})\rangle \sim 0.1$ km s^{-1} and $\langle (v(\text{Mg/Fe}) - v(\text{Ca II}))^2\rangle^{1/2} \sim 1.0$ km s^{-1}. Some of the discrepancies could be explained by systematic error differences among the various instruments or, more likely for the larger differences, the presence of unresolved blends. The large majority (87%) of velocity components agree to within 1.5 km s^{-1}.

3.2. *Doppler Parameter Distribution*

The observed value of the Doppler parameter (b) is a measure of the temperature (T) and turbulent velocity (ξ). The relationship is provided in equation (1). With the increase in atomic mass from magnesium to calcium to iron, the Doppler parameter becomes less influenced by thermal broadening and more influenced by turbulence or unresolved clouds along the line of sight. In Figure 5, the Doppler parameter distribution is plotted for all three ions, from the heaviest ion, Fe II, at the top, to the lightest ion, Mg II, at the bottom. A shift to larger line widths is seen in the Mg II distribution, indicating that thermal broadening is beginning to dominate the turbulent broadening for the lightest ion. The Fe II and Ca II distributions look very similar, probably because turbulent broadening dominates over the thermal broadening, thereby making the Doppler parameter independent of atomic mass. The mean Doppler parameter for the Fe II distribution is $\langle b(\text{Fe II})\rangle \sim 2.4$ km s^{-1} with a standard deviation of $\langle b^2(\text{Fe II})\rangle^{1/2} \sim 1.0$ km s^{-1}. We find similar values for Ca II: $\langle b(\text{Ca II})\rangle \sim 2.3$ km s^{-1} and $\langle b^2(\text{Ca II})\rangle^{1/2} \sim 1.2$ km s^{-1}. The Mg II distribution has a similar shape but is shifted to larger line widths: $\langle b(\text{Mg II})\rangle \sim 3.1$ km s^{-1} and $\langle b^2(\text{Mg II})\rangle^{1/2} \sim 0.8$ km s^{-1}. The high Doppler parameter tails for all three distributions likely results from unresolved multiple components. Observations with higher spectral resolution would help to disentangle the component structure and to fully resolve the

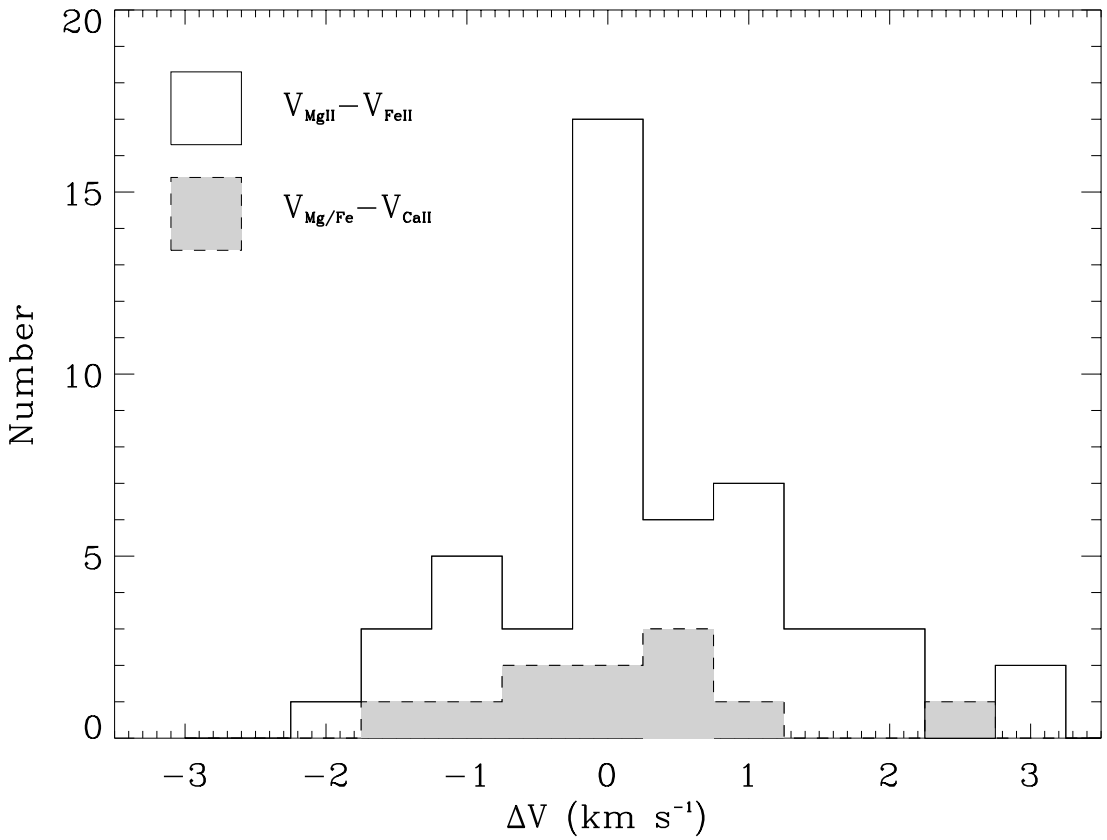

FIG. 4.—Distribution of the differences between the velocity components along the same line of sight observed with different ions. Of the 63 individual lines of sight observed in the UV in Table 1, 27 have both Mg II and Fe II observations, but with the 53 individual lines of sight observed in the optical and listed in Table 5, only seven have both optical Ca II and UV observations. The strong spike at zero velocity difference confirms the assumption that both Fe II and Mg II ions are tracing the same collection of gas in the LISM. While we have very few common velocity components between the optical Ca II and the UV ions, the results are similar. Some of the discrepancies could be explained by systematic error differences among the various instruments or the presence of unresolved blends. The large majority (87%) of velocity components agree to within 1.5 km s^{-1}. The bin size used is 0.5 km s^{-1}.

smallest line widths, enabling us to investigate more accurately the thermal and nonthermal characteristics of warm clouds in the LISM.

We compare in Figure 6 the Doppler parameter for the 27 sight lines with common velocity components in Mg II and Fe II spectra. The solid line indicates pure turbulent broadening, and the dashed line indicates pure thermal broadening. If the Mg II and Fe II ions are similarly distributed we would expect that $0.66 \leq b(\text{Fe II})/b(\text{Mg II}) \leq 1.0$ km s^{-1} and that all points would lie between the solid and dashed lines. Only five points out of 44 components lie outside the region by more than 1 σ. Of these five points, most are part of strong blends, making Doppler parameter measurements very difficult. Comparing the line widths of various atomic species with a range of atomic masses, is a powerful technique for measuring the temperature and turbulent velocity of clouds in the LISM. Analysis of interstellar absorption along these lines of sight by lighter ions, those least effected by nonthermal, turbulent broadening, will be studied in a future paper.

3.3. *Column Density Distribution*

The observed column density indicates the number of ions along the line of sight. If we assume a homogeneous medium with a constant density, the column density is directly proportional to the distance that the line of sight traverses through the cloud. The column density of individual absorption components provides information on the cloud thickness, an important measurement of the morphology of the LISM. The measured abundances also provide information on the degree of ionization and depletion of ions in the LISM. These characteristics can vary from cloud to cloud and even within a single cloud structure. In Figure 7, the *total* column density along a line of sight is plotted against distance to the observed target, the upper limit of the location of the absorbing cloud. Clearly, the distribution of material does not vary smoothly with distance. The dashed lines indicate column densities that would result from a spherical cloud of constant density, with a radius of 100 pc. The number density of Ca II is more than 2 orders of magnitude smaller than the number densities of Mg II and Fe II. Magnesium and iron have almost identical solar abundances, and both Mg II and Fe II are the dominant ionization species (Slavin & Frisch 2002). On the other hand, the calcium solar abundance is a factor of 10 lower than iron and magnesium (Anders & Grevesse 1989) and Ca III is the dominant ionization species for calcium in the warm LISM (Slavin & Frisch 2002). Together, these two effects can explain the column density differences between Ca II, on the one hand, and Fe II and Mg II on the other. This is also indicated by the ionization potentials of the three ions. Magnesium and iron have almost identical ionization potentials. Singly ionized magnesium requires 7.6 eV and iron 7.9 eV, while doubly ionized magnesium requires 15.0 eV and iron 16.2 eV. The ionization potentials for calcium are slightly

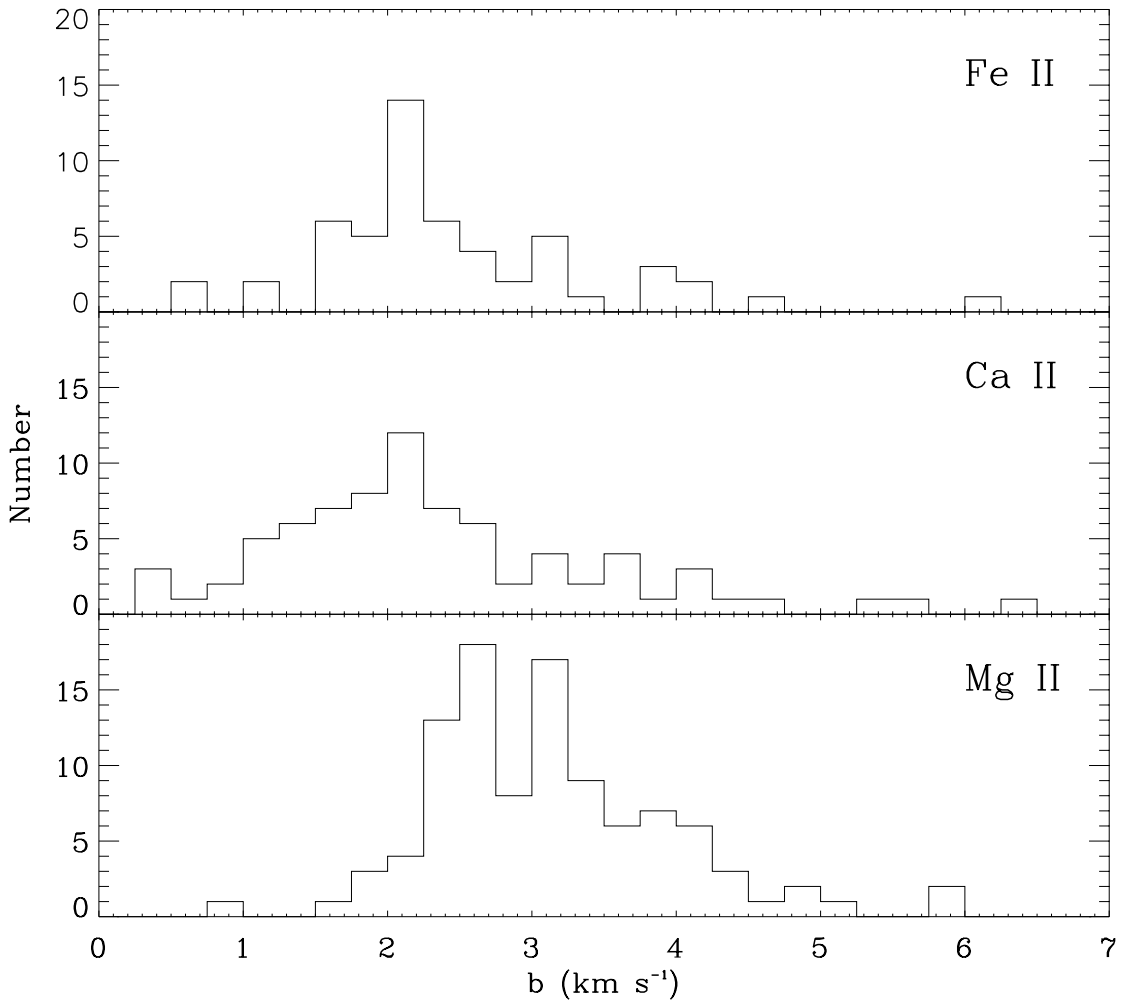

FIG. 5.—Doppler parameter distribution for all three ions, from the heaviest ion, Fe II, at the top, to the lightest ion, Mg II, at the bottom. The bin size used is 0.25 km s^{-1}. A clear shift to higher line widths is seen in the Mg II distribution, indicating that for the lightest ion thermal broadening is beginning to dominate the turbulent broadening. The Fe II and Ca II distributions look very similar and indicate that turbulent broadening dominates over thermal broadening, thereby making the Doppler parameter independent of atomic mass. The high Doppler parameter tails in all three distributions is likely the result of multiple components in unresolved blends.

lower. Singly ionized calcium requires 6.1 eV, while doubly ionized calcium requires 11.9 eV. The rich Hyades sample (Redfield & Linsky 2001) is clearly visible again in the Mg II panel at a distance of ~45 pc. Note that the total Mg II column densities for all 18 of the Hyades stars agree fairly well, but they are significantly different from targets at different distances. This indicates that the distribution of LISM material is clumpy and spatially correlated, dependent on the particular line of sight and the number of traversed clouds.

In Figure 8, the total column density for each of the three ions is shown in Galactic coordinates. The size of the symbol is inversely proportional to the target's distance, and the shading of the symbol indicates the total column density, as shown by the scale at the bottom of each plot. The total column density is clearly spatially correlated. As was found by Génova et al. (1990), the highest column densities tend to be in the southern Galactic center direction, and the lowest column densities tend to be in the northern anti–Galactic center direction. However, exceptions to this generalization exist. Good spatial coverage of the sky and of objects at various distances is crucial to understanding the morphology of the LISM. For example, β and σ Gem are only 1° apart on the sky, but β Gem is only 10.3 pc away, whereas σ Gem is 37.5 pc away. Their total Mg II column densities are almost identical, indicating that there is no additional Mg II material beyond 10.3 pc along the line of sight to σ Gem. Likewise, the different total Mg II column densities of Capella and G191-B2B (only 7° apart), indicate that there is more Mg II material beyond Capella at 12.9 pc in the direction toward G191-B2B at 68.8 pc.

The column density distribution for the individual clouds are given in Figure 9 for each ion. Both Fe II and Mg II have roughly the same column density, while typical Ca II column densities are lower by a factor of 100. As discussed above, this is a result of lower cosmic abundances of calcium and Ca II being a trace ionization species. The mean column density for Fe II is $\langle \log N(\mathrm{Fe\ II}) \rangle \sim 12.4$ with a standard deviation of $\langle \log N^2(\mathrm{Fe\ II}) \rangle^{1/2} \sim 0.5$. We find similar values for Mg II: $\langle \log N(\mathrm{Mg\ II}) \rangle \sim 12.6$ and $\langle \log N^2(\mathrm{Mg\ II}) \rangle^{1/2} \sim 0.6$. The Ca II distribution has a similar shape, but the mean column density is 2 orders of magnitude smaller than for Fe II and Mg II with $\langle \log N(\mathrm{Ca\ II}) \rangle \sim 10.4$ and $\langle \log N^2(\mathrm{Ca\ II}) \rangle^{1/2} \sim 0.4$. The small dispersion in the column

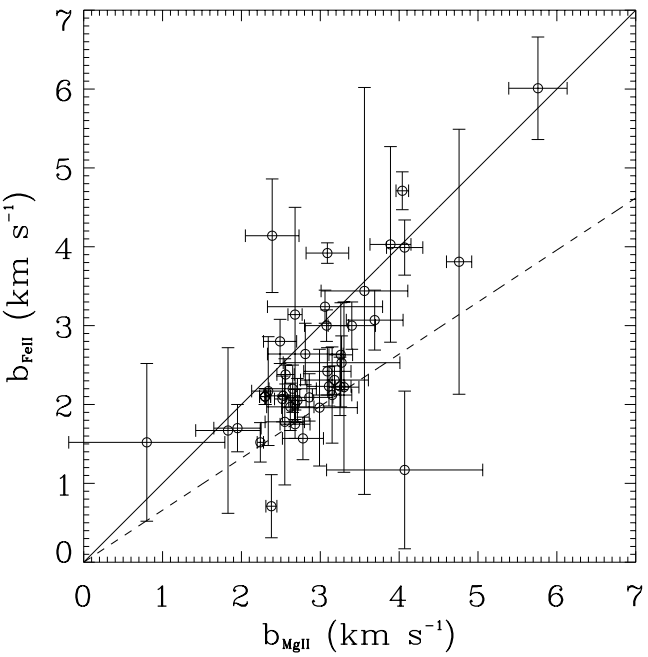

FIG. 6.—Comparison of Doppler parameters for the 27 sight lines with identical velocity components in Mg II and Fe II spectra. Error bars indicate 1 σ errors. The solid line indicates pure turbulent broadening, and the dashed line indicates pure thermal broadening. If the Mg II and Fe II ions are similarly distributed we would expect that all points would lie between the solid and dashed lines. Only five points out of 44 components lie outside the region by more than 1 σ.

densities suggests that nearby clouds in the LISM may have similar sizes. The dashed lines indicate LISM absorption detection limits for Fe II and Mg II spectra with a S/N $\sim$ 40, typical for these observations obtained with *HST*. As discussed above, the detection of weak lines is aided by spectra of multiple lines for single ions with different opacities. Therefore, the absolute detection limit for an individual line of sight will vary with S/N and which lines are observed. The low detection limit for the strong Mg II *h* and *k* lines indicates that it is possible to detect the weakest lines as long as they are not hidden in a blend with stronger absorption components. For a discussion of the detection limit typical for the optical Ca II observations, see Welty et al. (1996).

The column density is also important for determining the ionization structure and depletion characteristics of clouds in the LISM. In Figure 10 we compare the N(Fe II)/N(Mg II) ratio for the same velocity components. The dashed line is the Slavin & Frisch (2002) prediction of $\log[N(\text{Fe II})/N(\text{Mg II})] \sim -0.34$ at the solar location. Many of the components are consistent with their prediction. There is a suggestion of negative slope, possibly related to different rates of depletion onto grains for Mg II and Fe II.

4. CONCLUSIONS

Many fundamental questions regarding the physical structure of the LISM remain to be answered. What is the morphology of the LISM warm gas? Is it organized into clouds, or is it more chaotic and filamentary? What determines the motions of nearby gas? How does the history of the LISM determine its physical properties such as ionization and depletion? This paper will provide a database with which to analyze these important questions. We provide a

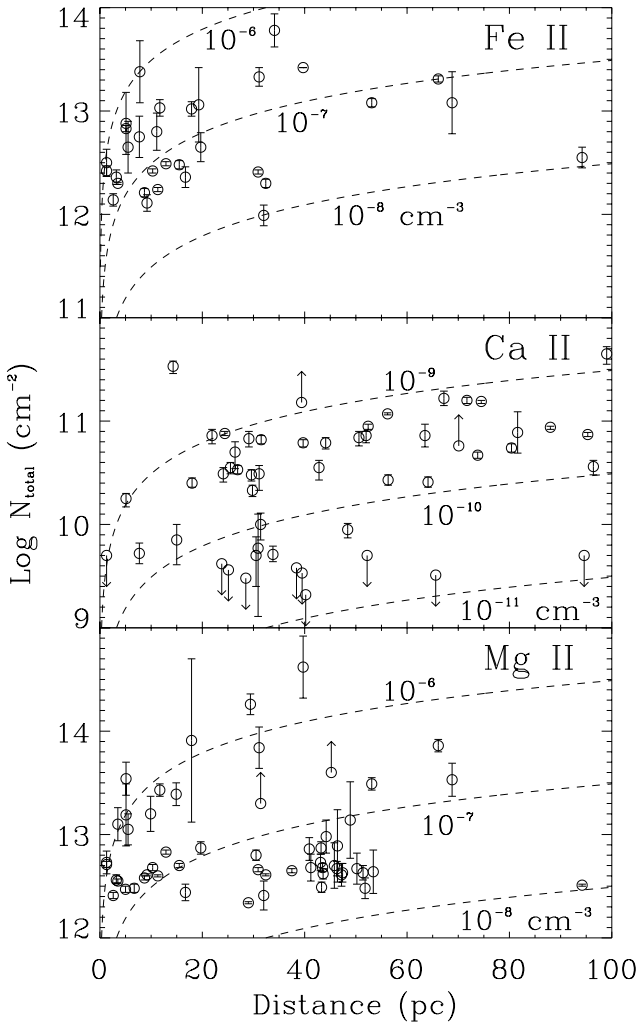

FIG. 7.—*Total* column density along a line of sight is plotted against the distance to the observed target, for all three ions. The dashed lines indicate column densities that result from a spherical cloud of constant density, with a radius of 100 pc. The number densities are given in units of cm^{-3}.

survey of all Mg II and Fe II high-resolution measurements, collecting data from the literature and analyzing the remaining unpublished results. Mg II and Fe II were analyzed first because they are heavy ions and provide the best determination of the velocity structure. Optical observations of Ca II were also included because Ca II is intermediate in mass between Mg II and Fe II, there are Ca II observations of additional lines of sight, and optical observations are often obtained with even higher spectral resolution than available in the UV on *HST*. All Ca II measurements were taken from the literature and provide additional information regarding the physical structure of the LISM. The accurate component velocity structure obtained here will be vital to analyzing the broader absorption components of the lighter ions.

Additional results presented here include determinations of the general characteristics of the LISM, such as the average column densities of nearby clouds. Comparisons of column densities provide information on the ionization and depletion structures in the LISM. We find that the abundance ratio of Mg II and Fe II varies from cloud to cloud. The comparison of the Doppler parameters for Fe II and Mg II indicate that these ions coexist in the same clouds of warm gas, unlike Ca II and Na I (Welty et al. 1996). Ca II

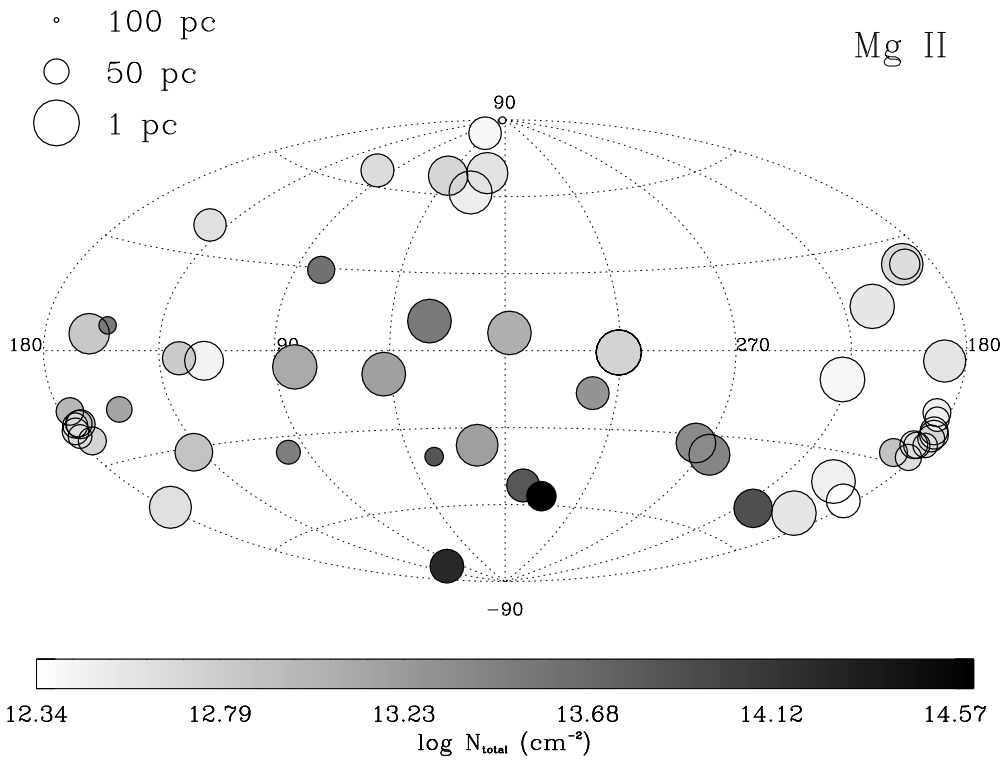

FIG. 8.—Total column density for all three ions are shown in Galactic coordinates. The size of each symbol is inversely proportional to the distance, and the shading of the symbol indicates the total column density, as shown by the scale at the bottom of each plot. The total column densities are clearly spatially correlated. The highest column densities tend to be in the southern Galactic center direction, and the lowest column densities tend to be in the northern anti–Galactic center direction.

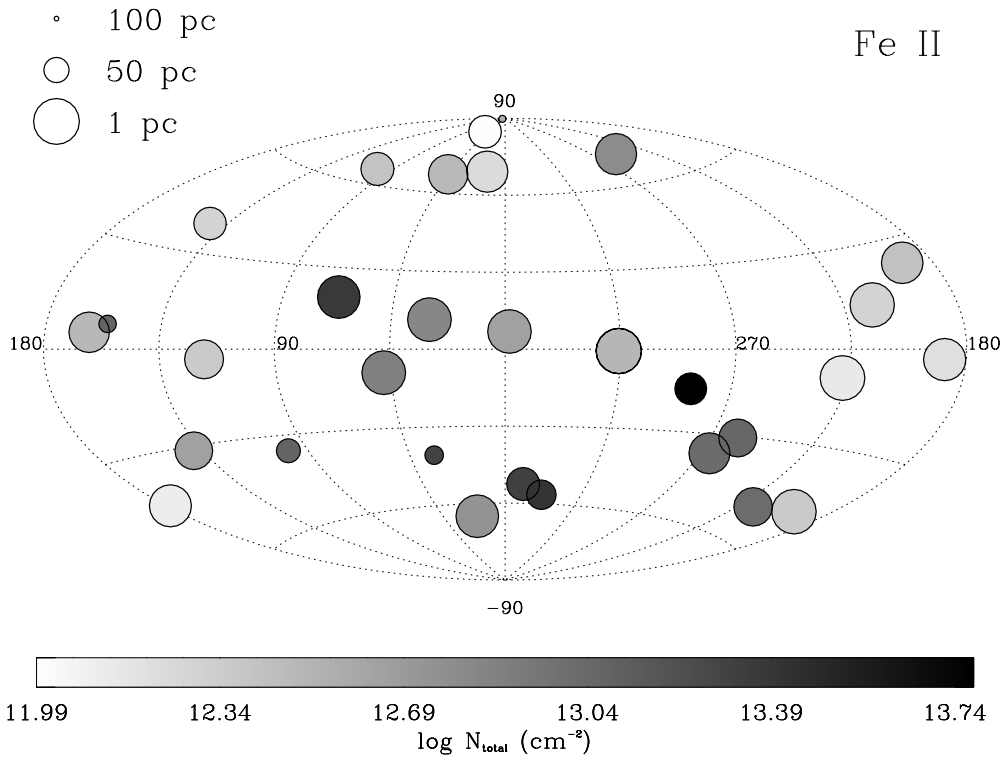

FIG. 8.—*Continued*

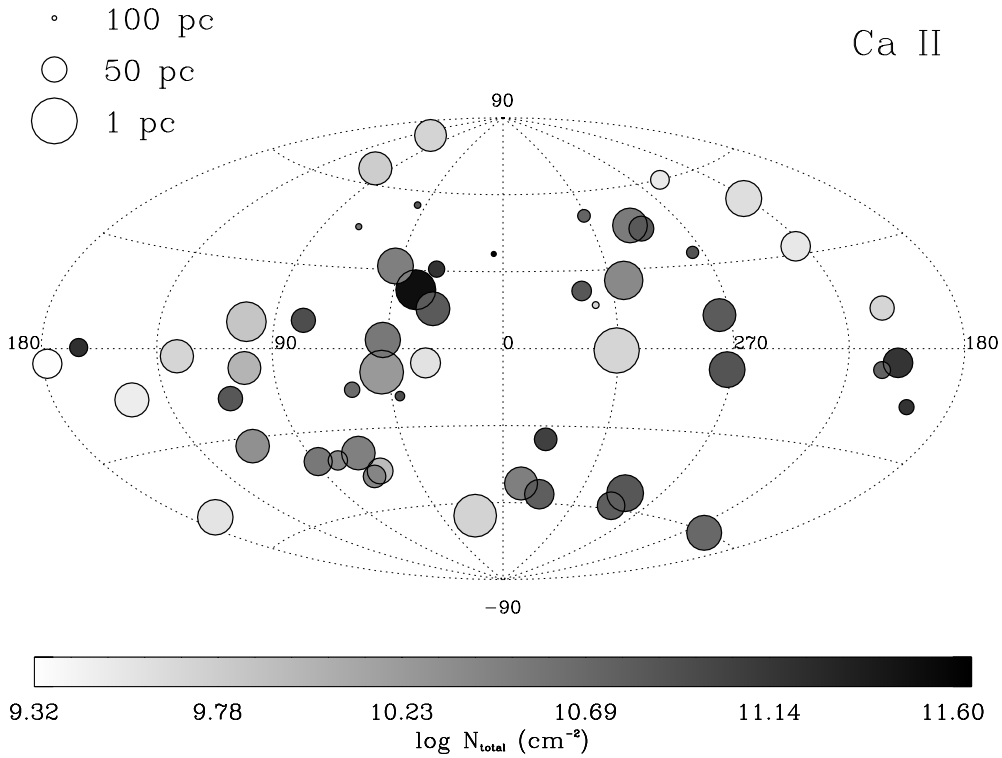

FIG. 8.—*Continued*

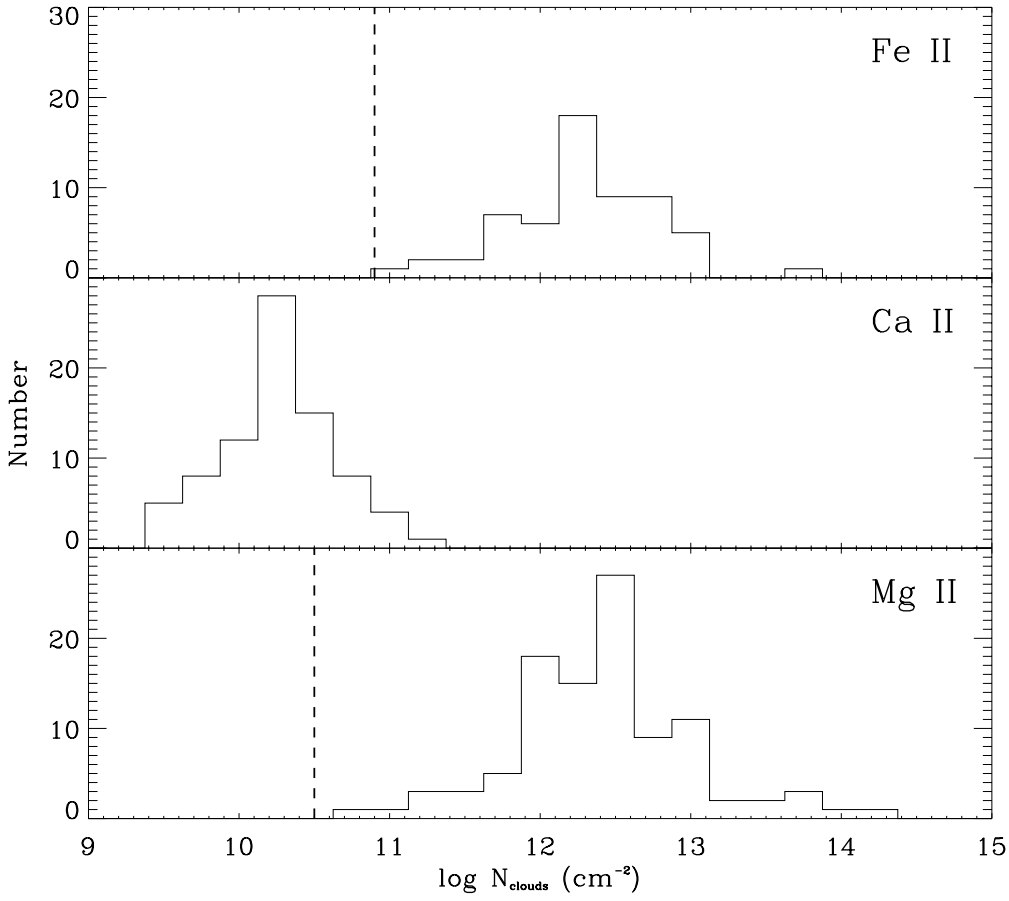

FIG. 9.—Column density distribution for individual clouds are given for each ion. Both Fe II and Mg II have roughly the same column densities, while typical Ca II column densities are lower by a factor of 100. The dashed lines indicate LISM absorption detection limits for Fe II and Mg II spectra with a S/N $\sim$ 40, typical for these observations obtained with *HST*.

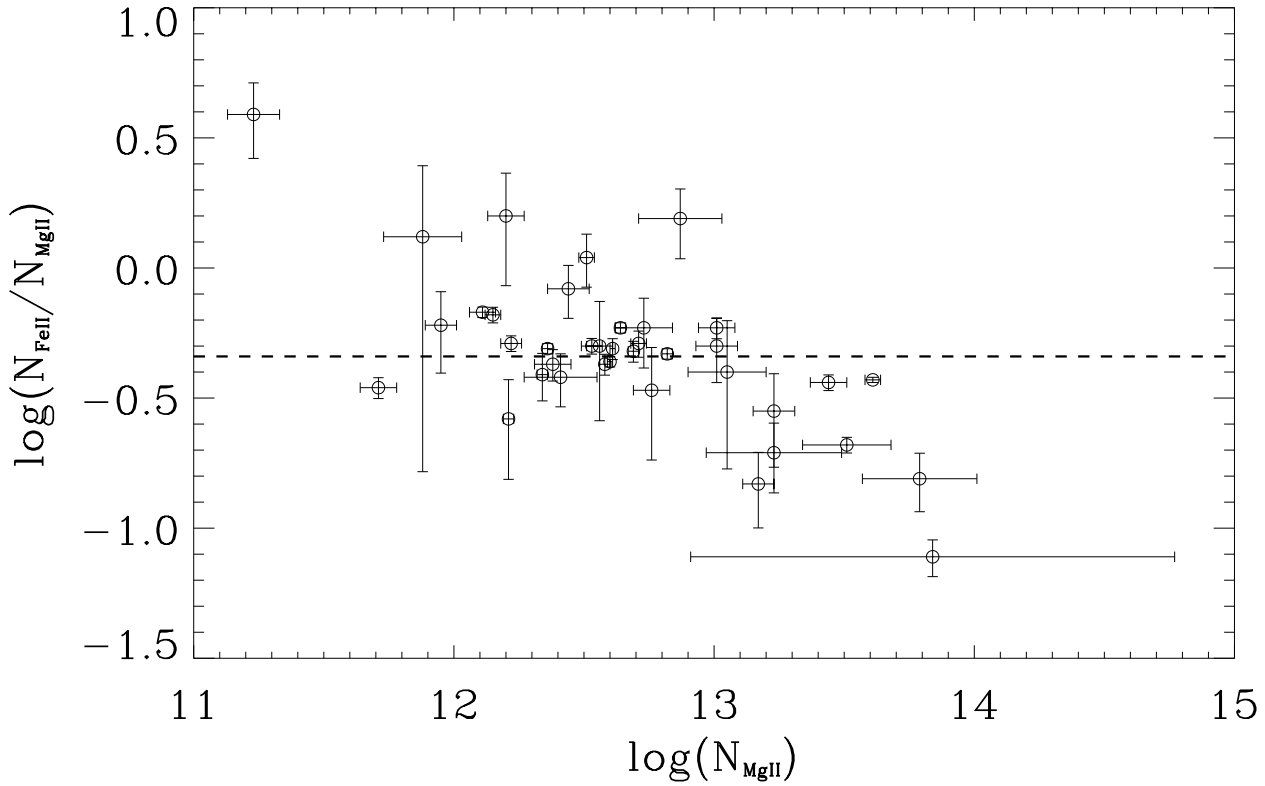

FIG. 10.—Abundance ratio of Fe II to Mg II, as a function of Mg II column density. The dashed line is the Slavin & Frisch (2002) prediction of $\log N(\text{Fe II})/N(\text{Mg II}) \sim -0.34$ at the solar location. Many of the components are consistent with their prediction. There is an indication of negative slope, possibly related to different rates of depletion onto grains for Mg II and Fe II.

absorption appears to coexist with Mg II and Fe II in the LISM, although unlike Mg II and Fe II it is not the dominant ion state. A comparison of the Doppler parameters of the heavy ions presented here, with the lighter ions in the same line of sight, will lead to accurate measurements of the temperature and turbulent velocity of individual clouds. We find that the velocity measurements of Mg II and Fe II absorption agree fairly well, but discrepancies still exist. These are most likely due to discrepancies between the absolute wavelength scales among the different instruments used. However, the undetected presence of unresolved blends could be an important cause of these discrepancies as well. Welty et al. (1996) present an argument that even the highest resolution spectrographs are not capable of discerning half of the velocity components. This argument is based on the assumptions that the true sample of component velocities in the LISM are uncorrelated and obey a single Poisson distribution. Observations with even higher resolution spectrographs in the UV and optical are required to determine whether these assumptions are valid.

Future work involves providing a similar database of the light ions. A complete UV survey of LISM lines will provide invaluable insights into the physical properties of the LISM, such as, kinematics, temperature, turbulent velocity, depletion, and ionization structure. Observations in the far-ultraviolet with the *Far Ultraviolet Spectroscopic Explorer* (*FUSE*) will provide measurements of important ions that are not present in the spectral range of *HST* or in the optical. By going beyond the single sight line approach of LISM analysis, we will finally be able to answer some of the fundamental questions about the nearest interstellar environment.

This research is supported by NASA grants NGT5-50242 and S-56500-D to the University of Colorado at Boulder.

REFERENCES

Anders, E., & Grevesse, N. 1989, Geochim. Cosmochim. Acta, 53, 197
Artymowicz, P. 1997, Annu. Rev. Earth Planet. Sci., 25, 175
Bertin, P., Lallement, R., Ferlet, R., & Vidal-Madjar, A. 1993, A&A, 278, 549
Brandt, J. C., et al. 1994, PASP, 106, 890
Brandt, J. C., et al. 2001, ApJ, 121, 2173
Carpenter, K. G., Robinson, R. D., & Judge, P. G. 1995, ApJ, 444, 424
Centurion, M., & Vladilo, G. 1991, ApJ, 372, 494
Cox, D. P., & Reynolds, R. J. 1987, ARA&A, 25, 303
Crawford, I. A. 1994, Observatory, 114, 288
Crawford, I. A., Craig, N., & Welsh, B. Y. 1997, A&A, 317, 889
Crawford, I. A., & Dunkin, S. K. 1995, MNRAS, 273, 219
Crawford, I. A., Lallement, R., & Welsh, B. Y. 1998, MNRAS, 300, 1181
Crutcher, R. M. 1982, ApJ, 254, 82
Dehnen, W., & Binney, J. J. 1998, MNRAS, 298, 387
Dring, A. R., Linsky, J. L., Murthy, J., Henry, R. C., Moos, W., Vidal-Madjar, A., Audouze, J., & Landsman, W. 1997, ApJ, 488, 760
Duflot, M., Figon, P., & Meyssonnier, N. 1995, A&AS, 114, 269
Ferlet, R., Lallement, R., & Vidal-Madjar, A. 1986, A&A, 163, 204
Ferlet, R., Lecavelier des Etangs, A., Vidal-Madjar, A., Bertin, P., Deleuil, M., Lagrange-Henri, A.-M., & Lallement, R. 1995, A&A, 297, L5
Frisch, P. C. 1987, ApJS, 65, 313
———. 1995, Space Sci. Rev., 72, 499
Frisch, P. C., Jenkins, E. B., Welty, D. E., & Johns-Krull, C. 1999, BAAS, 31, 947
Génova, R., Molaro, P., Vladilo, G., & Beckman, J. E. 1990, ApJ, 355, 150
Gilliland, R. L. 1994, GHRS Instrum. Sci. Rep. 063 (Baltimore: STScI)
Heap, S. R., et al. 1995, PASP, 107, 871

Kimble, R. A., et al. 1998, ApJ, 492, L83
Lagrange-Henri, A. M., Ferlet, R., Vidal-Madjar, A., & Beust, H. 1991, A&A, 246, 507
Lallement, R., & Bertin, P. 1992, A&A, 266, 479
Lallement, R., Bertin, P., Ferlet, R., Vidal-Madjar, A., & Bertaux, J. L. 1994, A&A, 286, 898
Lallement, R., & Ferlet, R. 1997, A&A, 324, 1105
Lallement, R., Ferlet, R., Lagrange, A. M., Lemoine, M., & Vidal-Madjar, A. 1995, A&A, 304, 461
Lallement, R., Vidal-Madjar, A., & Ferlet, R. 1986, A&A, 168, 225
Lecavelier des Etangs, A., et al. 1997, A&A, 325, 228
Lemoine, M., Vidal-Madjar, A., Bertin, P., Ferlet, R., Gry, C., & Lallement, R. 1996, A&A, 308, 601
Lindler, D. 1999, CALSTIS Reference Guide (Greenbelt: NASA/LASP)
Linsky, J. L., et al. 1993, ApJ, 402, 694
Linsky, J. L., Diplas, A., Wood, B. E., Brown, A., Ayres, T. R., & Savage, B. D. 1995, ApJ, 451, 335
Linsky, J. L., Redfield, S., Wood, B. E., & Piskunov, N. 2000, ApJ, 528, 756
Linsky, J. L., & Wood, B. E. 1996, ApJ, 463, 254
Morton, D. C. 1991, ApJS, 77, 119
Perryman, M. A. C., et al. 1997, A&A, 323, L49
Piskunov, N., Wood, B. E., Linsky, J. L., Dempsey, R. C., & Ayres, T. R. 1997, ApJ, 474, 315
Redfield, S., & Linsky, J. L. 2000, ApJ, 534, 825
———. 2001, ApJ, 551, 413
Reid, N., & Wegner, G. 1988, ApJ, 335, 953
Robinson, R. D., Blackwell, J., Feggans, K., Lindler, D., Norman, D., & Shore, S. N. 1992, A User's Guide to the GHRS Software, Version 2.0 (Greenbelt: Goddard Space Flight Center)
Robinson, R. D., & Carpenter, K. G. 1995, ApJ, 442, 328
Robinson, R. D., Carpenter, K. G., & Brown, A. 1998, ApJ, 503, 396
Sahu, K. C., et al. 1999, STIS Instrument Handbook (Baltimore: STScI)
Sahu, M. S., Blades, J. C., He, L., Hartmann, D., Barlow, M. J., & Crawford, I. A. 1998, ApJ, 504, 522
Savage, B. D., & Sembach, K. R. 1996, ARA&A, 34, 279
Sfeir, D. M., Lallement, R., Crifo, F., & Welsh, B. Y. 1999, A&A, 346, 785
Slavin, J. D., & Frisch, P. C. 2002, ApJ, 565, 364
Soderblom, D. R., Hulbert, S. J., Leitherer, C., & Sherbert, L. E. 1994, *HST* Goddard High Resolution Spectrograph Instrument Handbook, Version 5.0 (Baltimore: STScI)
Vallerga, J. V., Vedder, P. W., Craig, N., & Welsh, B. Y. 1993, ApJ, 411, 729
Vennes, S., & Thorstensen, J. R. 1994, AJ, 108, 1881
Vidal-Madjar, A., et al. 1994, A&A, 290, 245
Vidal-Madjar, A., Lecavelier des Etangs, A., & Ferlet, R. 1998, Planet. Space Sci., 46, 629
Welsh, B. Y., Craig, N., Vedder, P. W., & Vallerga, J. V. 1994, ApJ, 437, 638
Welsh, B. Y., Crifo, R., & Lallement, R. 1998, A&A, 333, 101
Welty, D. E., Hobbs, L. M., & Kulkarni, V. P. 1994, ApJ, 436, 152
Welty, D. E., Morton, D. C., & Hobbs, L. M. 1996, ApJS, 106, 533
Witte, M., Rosenbauer, H., Banaszkewicz, M., & Fahr, H. 1993, Adv. Space Res., 13, 121
Wood, B. E., & Linsky, J. L. 1998, ApJ, 492, 788
Wood, B. E., Linsky, J. L., & Zank, G. P. 2000, ApJ, 537, 304
Wood, B. E., Müller, H.-R., & Zank, G. P. 2000, ApJ, 542, 493
Woodgate, B. E., et al. 1998, PASP, 110, 1183